Journal of Natural Gas Science and Engineering 95 (2021) 104157

Contents lists available at ScienceDirect

Journal of Natural Gas Science and Engineering

journal homepage: www.elsevier.com/locate/jngse

Gas permeability and fracture compressibility for proppant-supported shale fractures under high stress

Tianyu Chen [a], Yanji Fu [b], Xia-Ting Feng [a,*], Yuling Tan [c,d], Guanglei Cui [a], Derek Elsworth [e], Zhejun Pan [f,**]

[a] Key Laboratory of Ministry of Education on Safe Mining of Deep Metal Mines, Northeastern University, Shenyang, 110004, China
[b] Department of Civil Engineering, Liaoning Technical University, Fuxin, 123000, China
[c] Department of Engineering Mechanics, Shijiazhuang Tiedao University, Shijiazhuang, 050043, China
[d] Hebei Key Laboratory of Mechanics of Intelligent Materials and Structures, Shijiazhuang Tiedao University, Shijiazhuang, 050043, China
[e] Department of Energy and Mineral Engineering, EMS Energy Institute and G3 Center, Pennsylvania State University, University Park, PA, 16802, USA
[f] CSIRO Energy Business Unit, Private Bag 10, Clayton South, VIC, 3169, Australia

ARTICLE INFO

Keywords:
Gas shales
Proppant
High stress
Permeability
Compressibility

ABSTRACT

Proppants hold fractures open and increase fracture conductivity but must survive and remain functional during pressure drawdown. The shale reservoir usually suffers a high effective stress during gas depletion whilst most previous experiment works are conducted under a relative low stress level. In this work, permeability evolution was explored in a proppant-supported natural fracture of Longmaxi shale from the Sichuan Basin, China under a large effective stress range (1.5–59.5 MPa). Proppant performance was examined via continuous permeability measurements and by optical microscopy and laser-classifier measurements of particle size distributions (PSD) recored both pre- and post-loading. The permeability of the propped shale fracture is two orders of magnitude higher than that of the non-propped fracture and strongly controlled by the proppant behaviour. Surprisingly, overall permeability of the proppant pack decreases with an increase in thickness of the enclosed proppant. The decrease in the permeability with high stresses is largest for unpropped fractures and decreases with an increase in the number of layers. Most important, the mean compressibility of the non-propped and propped fracture is not constant but reduces with an increase in confining stress. This indicates that the compaction, crushing, embedment and repacking of the proppant particles, because of high effective stress, resulting in a decrease in the porosity of the proppant pack further reducing the compressibility and permeability of the supported fracture.

1. Introduction

The permeability of the artificial fractures created by hydraulic fracturing and retained open by the remnant proppant pack (Pangilinan et al., 2016; Wang and Elsworth, 2018) is one of the main factors controlling economic production of shale gas (Alramahi and Sundberg, 2012; Cui et al., 2018a). Furthermore, the effective stress ultimately increases during the flowback of the fracturing fluid (Cui et al., 2020b) and subsequent reservoir pressure drawdown – enabling fracture and proppant compaction (Chen et al., 2017; Cui et al., 2018b; Fan et al., 2017). This may result both in the further decrease in fracture width and the reduction in permeability (up to 95 %) of the proppant pack (Han and Wang, 2014; Li et al., 2016; Palisch et al., 2007) – impacting gas production. Hence, understanding proppant behaviour under high effective stress and its effect on fracture permeability is important in reservoir management and in maximizing gas production.

Rock properties, proppant arrangement and layers all affect propped fracture permeability and the interaction between proppant and rock (Cutler et al., 1985; Herskovits et al., 2016; Mittal et al., 2017; Volk et al., 1981). Multilayer proppant arrangement may allow more contact points to resist stress, which can reduce proppant breakage caused by stress and ensure minimal loss of proppant pack conductivity (Elsarawy and Nasr-El-Din, 2018). Proppant crushing and the generation of fines is a primary mode of permeability destruction in hard rocks (Lacy et al.,

* Corresponding author.
** Corresponding author.
E-mail addresses: xiatingfeng@mail.neu.edu.cn (X.-T. Feng), Zhejun.Pan@csiro.au (Z. Pan).

https://doi.org/10.1016/j.jngse.2021.104157
Received 4 November 2020; Received in revised form 6 June 2021; Accepted 20 July 2021
Available online 22 July 2021

Table 1
Summarization of related works.

S_c, MPa	S_a, MPa	p_s, MPa	Sample material	Proppant type	c	k	Literature
9	20	–	Coal/shale		5	–	Zhi and Elsworth (2020)
34.5	34.5	–	Shale	Resin-coated sand	1	–	Arshadi et al. (2018)
70	70	–	Shale	Sand/sintered bauxite	1	–	Elsarawy and Nasr-El-Din (2018)
70	70	–	Steel/shale/sandstone	Coated sand/Ceramic/quartz	1	–	Hou et al. (2017)
86	86	–	Steel	Ceramic/sand	4	–	Man and Wong (2017)
25	25	2–13	Granite/shale	Ceramic	1	10^{-16}-10^{-14}	Hou et al. (2020)
16	16	9	Coal	Glass/Sand	1	10^{-14}–10^{-13}	Wu et al. (2018)
2.57	9	6.8	Shale	Glass beads/sand	1	10^{-15}–10^{-13}	Tan et al. (2018)
20	20	12	Shale	Carbolite	1	~10^{-15}	Li et al. (2017)
10	10	6	Coal	Quartz sand	1	10^{-15}–10^{-13}	Kumar et al. (2015)

In the table, S_c represents the confining pressure, S_a denotes the axial loading pressure, p_s means the saturant pressure, c denotes the loading cycle, k represents the measured permeability.

Table 2
Geochemical properties of the shale samples.

Mineral compositions (%)						TOC (%)	$R_{o,max}$ (%)
Quartz	Feldspar	Pyrite	Clay minerals	Calcite	Dolomite		
32.45	3.42	3.13	18.57	32.16	8.02	2.24	2.41

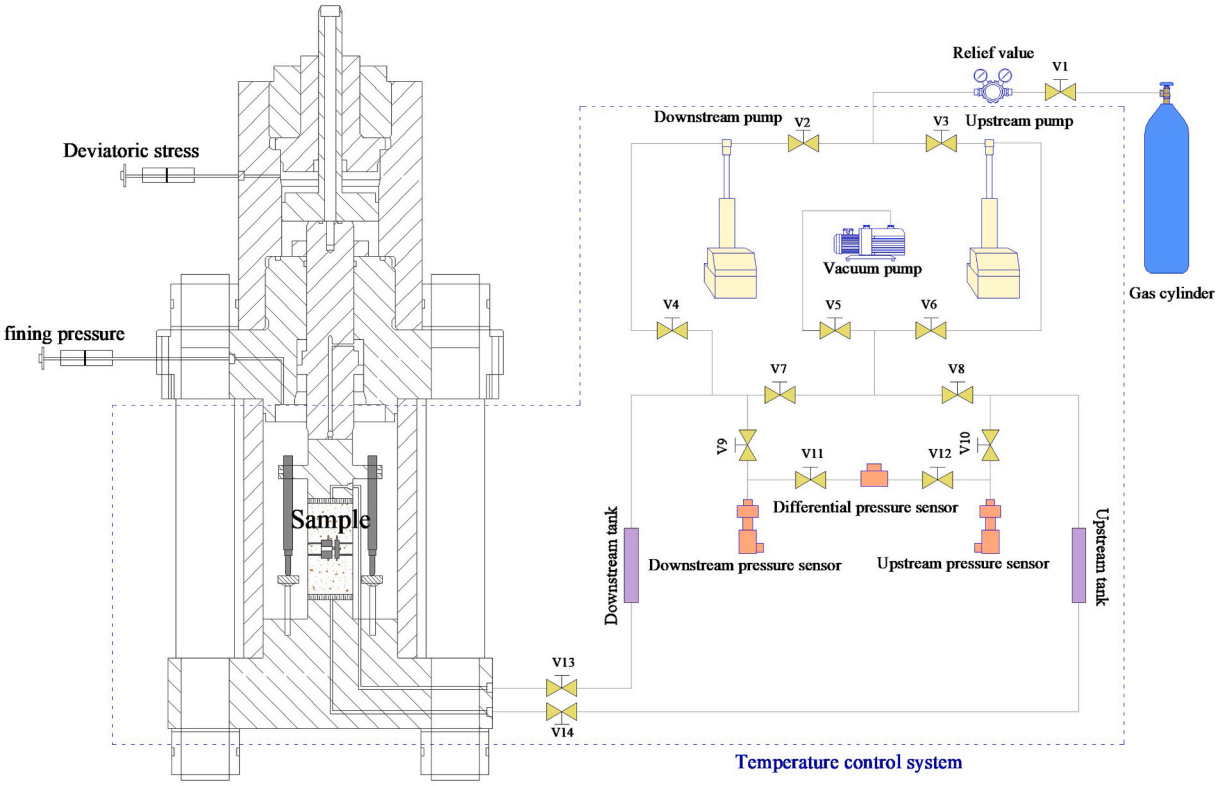

Fig. 1. Schematic diagram of the experimental setup.

1997) while embedment in soft rocks typically shields destruction of the proppant itself until stresses become very high (Wen et al., 2007). Thus, the increased number of proppant layer may also result in denser packing and a reduction in pore throat diameter and porosity at high stress, potentially reducing permeability (Man and Wong, 2017). The permeability evolution of proppant supported fractures is highly sensitive to the change of stress (Shamsi et al., 2017). Several orders of magnitude reduction in proppant conductivity can be found as the stress increases (Cooke, 1973; Dusterhoft et al., 2004; Fredd et al., 2001). Although widely studied, it is difficult to define the key processes influencing the performance of proppants and permeability evolution, and experimental studies in the laboratory are essential to improve fundamental understanding.

Many authors have conducted displacement-controlled diametrical compression tests to the understanding of embedment and compression behaviour of proppant (Hou et al., 2017; Man and Wong, 2017). The single proppant grain and proppant pack are successively tested and steel plate are applied to simulate the rock fracture (Arshadi et al., 2018). In this approach, the interaction in inner proppants and between proppant and host rock are poorly considered and the permeabilities are not measured. To make up this defect, the real rock sample are used to investigate the impact of embedment and compression behaviour of

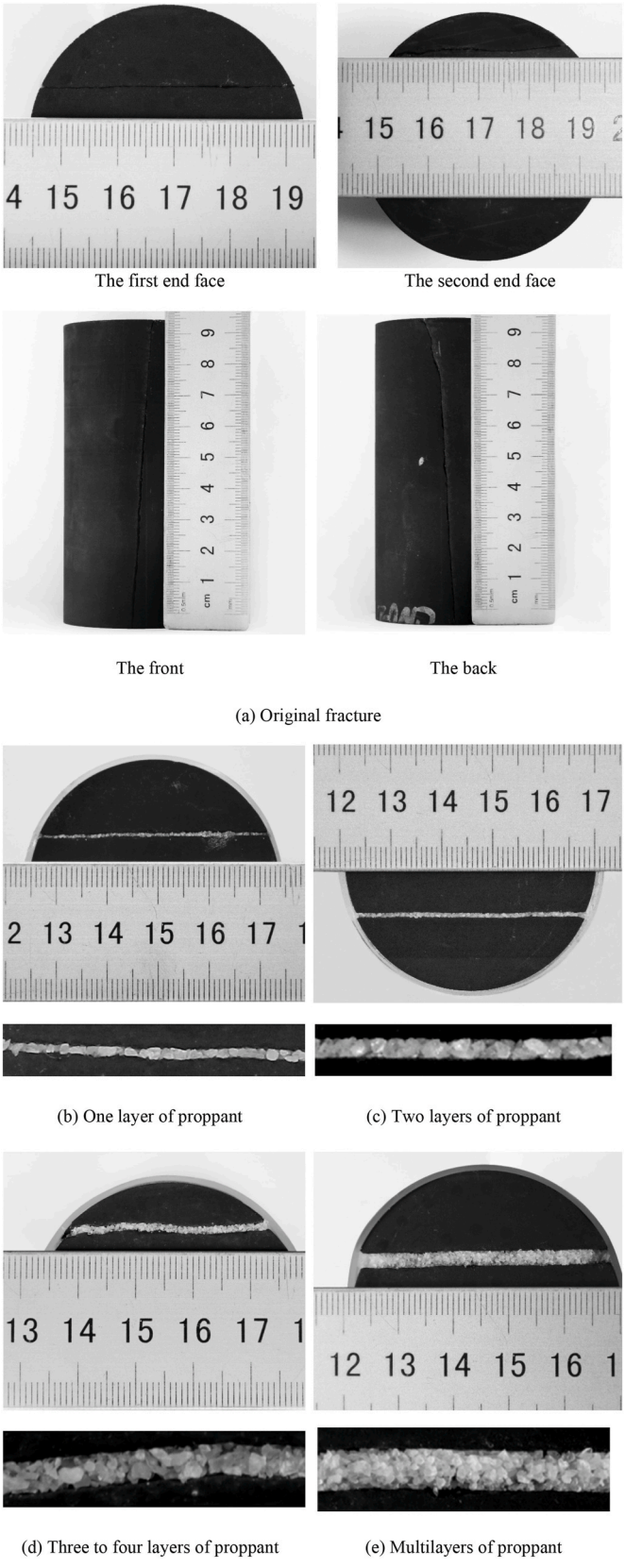

Fig. 2. Longmaxi shale sample with the original natural fracture and containing different layer thicknesses (number of layers of) proppant (sand).

proppant on permeability variation (Li et al., 2017). Wan and Tan conducted a series of experimental work to specify the coal/shale permeability evolution with different proppant type and layer (Tan et al., 2018; Wu et al., 2018). The impact of gas adsorption behaviour on the proppant permeability were also determined by Zhi and Elsworth (2020). The summarize of related works is listed in Table 1.

Although the permeability of propped artificial fractures has been extensively explored experimentally, the response of proppant packs under the high stresses anticipated in many reservoirs and under complete pressure drawdown remains poorly defined. (i) High in-situ stresses are manifest in deep shale gas reservoirs, inducing changes in the fracture aperture as the proppant grains undergo deformation, crushing and embedment. This associated proppant deformation causes an increase in angularity of the proppant grains, decrease in particle size and the potential for the clogging of pores and permeability reduction in the propped fracture; (ii) Studies using metal and sandstone "fractures" do not replicate the conditions of real shale reservoirs where embedment and damage and comminution of the surrounding fractures contribute to the loss of function of the proppant pack (Mittal et al., 2017). (iii) In addition, existing proppant studies are mostly carried out using artificial parallel steel plate fractures. Measurements using flat, parallel core faces tend to overestimate the conductivity of hydraulic fractures (Fredd et al., 2000) and natural propped fractures formed in shear and tension (Kassis and Sondergeld, 2010; Raimbay et al., 2016).

To overcome these many shortcomings, a natural fracture of Longmaxi shale (Sichuan Basin, China) is selected as a surrogate for a fluid-driven artificial fracture to explore key factors controlling permeability evolution in proppant-supported fractures at high-stress in shale. The evolution of Helium (He) permeability is measured for un-propped and propped fractures at effective stresses up to 59.5 MPa. In particular, the effects of stress cycling and the number of proppant layers on fracture permeability are investigated. Proppant distribution and morphology is imaged within the fracture by non-destructive X-ray CT following the permeability measurement. The variation of proppant morphology and fracture surface characteristics are observed post-experiment via optical microscopy with changes in the proppant particle-size-distribution recovered from a laser PSD classifier. Finally, fracture compressibilities are obtained by modelling experimental data using different permeability models. The relationships between high stress, proppant layers and compressibility are described.

2. Experimental

Layered proppant distributed within a cored natural fracture in Longmaxi shale is used as an analogue for a propped hydraulic fracture. Permeability is measured on the proppant-filled longitudinally-split core under variable stresses and with variable thicknesses of the proppant pack to determine the key dependencies.

2.1. Samples

The shale sample used in this work was recovered from an outcrop of the Silurian Longmaxi formation of the Sichuan Basin in southwest China. Fresh shale blocks were selected and transported to the laboratory. A shale core sample, 5 cm in diameter and 10 cm in height, was drilled along bedding. The core sample has a single longitudinal natural fracture separating the core into two pieces. The evolution of fracture permeability was measured both with and without proppants using this sample. Offcut samples were used for measurements of organic carbon content, maturity and mineral composition. The geochemical parameters of the shale are shown in Table 2. The weight of the sample is 490.48g.

2.2. Experiment methods

Quartz sand is a widely used proppant because of its low cost and

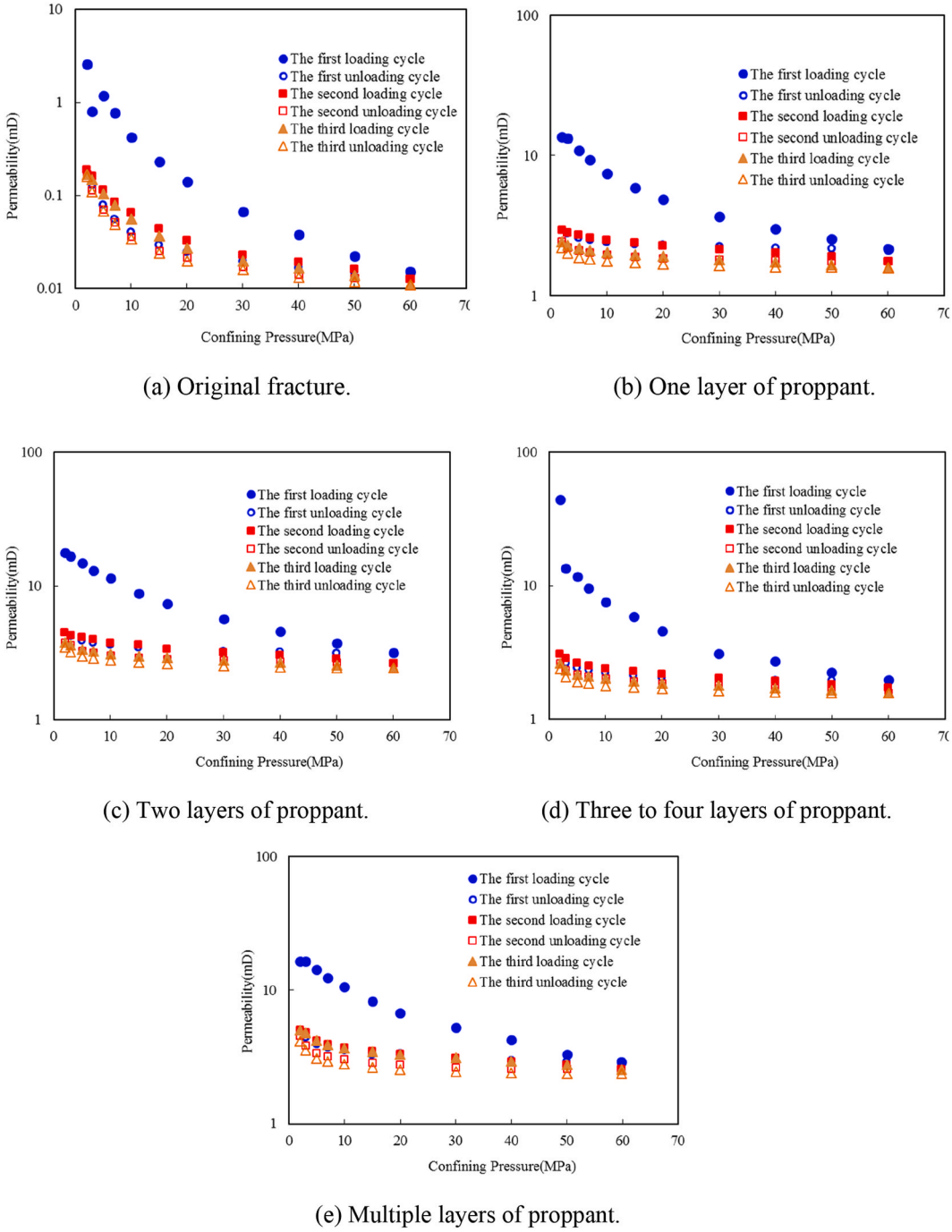

Fig. 3. The permeability of shale fracture both without proppant (a) and with different numbers of layers of proppant ((b)–(e)) (solid symbol: the permeability during the loading cycle; hollow symbol: the permeability during the unloading cycle).

inert response (Yang and Economides, 2012; Zheng et al., 2018). Quartz with a particle size distribution between #30 to #50 mesh, which is typically used in the field operations, was used in this work. Mineral density of the sand was measured by pycnometer (2649 kg/m^3) and the particle size distribution of the sand was determined by laser classifier. In order to avoid breakage of proppant particles, wet dispersion was selected for particle dispersion during proppant particle size measurement, and pure water was used as the medium for dispersing proppant particles. The mixture of proppant particles and dispersible media was evenly transported by ultrasound to the sample pool to test the particle size distribution. In order to calculate the porosity of proppants within the fracture, the sample was wrapped in a transparent thermal shrink-wrap sleeve before the proppants was filled into the fracture. The volume of the sample and combined shrink-wrap sleeve was measured by a three-dimensional laser scanning. Then the thermal-shrink-wrap sleeve was removed, and the sample opened. The total weight of the sand used for proppant experiments was measured before proppant filling.

The proppant packs were assembled by moistening the sand into a paste and laying that paste evenly on the fracture surface (Tan et al., 2018). The number of proppant layers can be determined by the sand grain distribution at the end face of the sample. The thickness of sand grains in the fracture is considered consistent as the number of layers at both end faces are the same. However, it should be noted that the

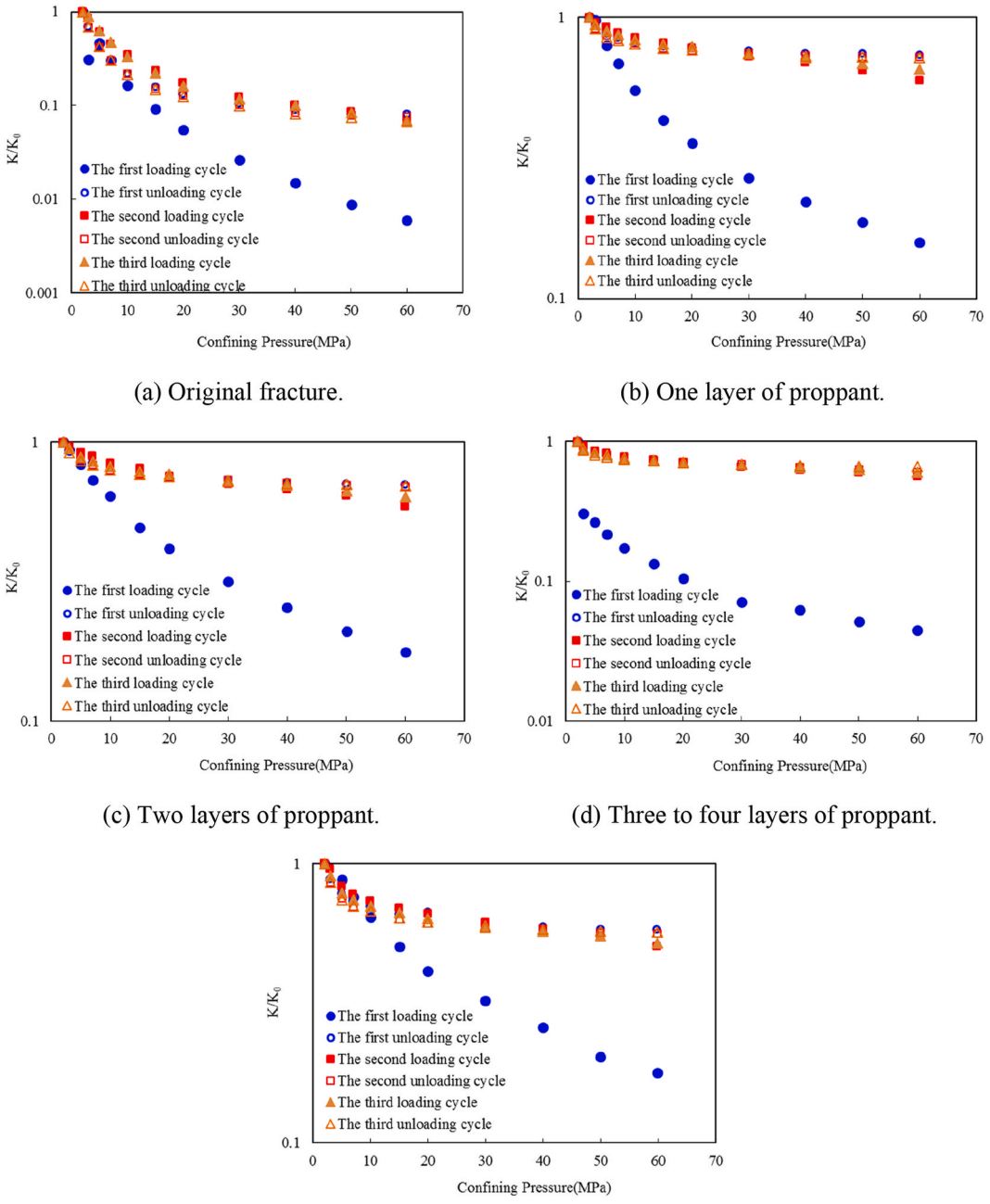

Fig. 4. Permeability ratio of shale fracture both without proppant (a) and with different numbers of layers of proppant ((b)–(e)) (solid symbol: the permeability ratio during the loading cycle; hollow symbol: the permeability ratio during the unloading cycle).

thickness of proppant particles in the fracture may be uneven due to the roughness of the fracture surface. The contact and the void distribution between proppant particles on the fracture surface were recorded and photographed with the ultra-depth-of field-optical microscope prior to permeability measurements. Then the two pieces of the core sample were mated with the sand proppant sandwiched within the fracture. The core sample was then wrapped with the transparent thermal-shrink-wrap sleeve and the bottom of the sample encapsulated with filter paper to avoid migration and loss of the sand particles from the fracture. The sample containing the sand proppant was then dried in a vacuum oven until its weight did not change. Then the sample was shaken to allow the dry sand particles to accumulate at the base of the fracture and dry sand filled into the fracture void from the top of the fracture. When the fracture was fully filled with dry sand, the top end face was photographed. The volume of the sample with proppant and the thermal-shrink-wrap sleeve was again measured by the laser scanner. The fracture volume is calculated by subtracting the volume of the sample without proppants from that with proppants. The weight of the sand filling in the fracture is then calculated by subtracting the weight of the sands after proppant filling from that before proppant filling. Proppant porosity can be calculated as (Tan et al., 2017):

$$\varphi_{\mathrm{p}} = 1 - \frac{m_s/\rho_{\mathrm{s}}}{V_{\mathrm{F}}} \tag{1}$$

where ϕ_p is the porosity of the proppant-propped fracture, m_s is the weight of the sand filling the fracture, kg; ρ_s is the true density of the

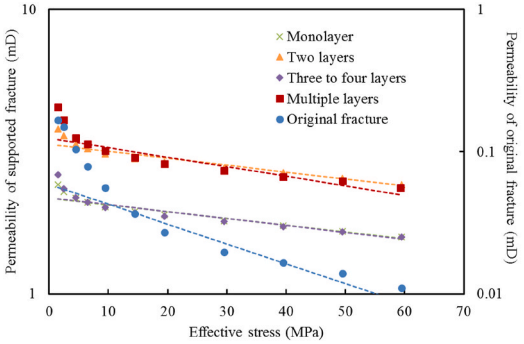

(a) The permeability of a propped fracture with different numbers of layers of proppant for the third loading cycle using Eq. (4).

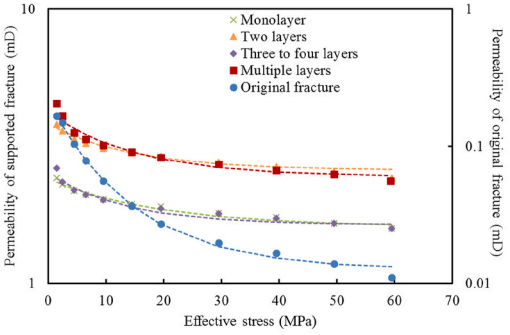

(b) Modeling results using Eq. (6).

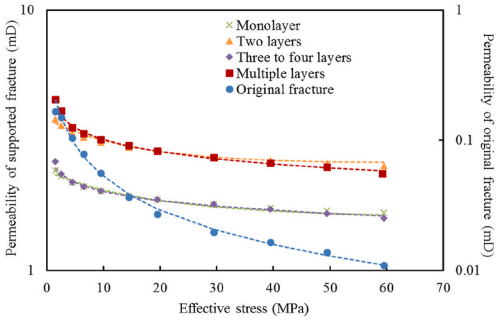

(c) Modeling results using Eq. (8).

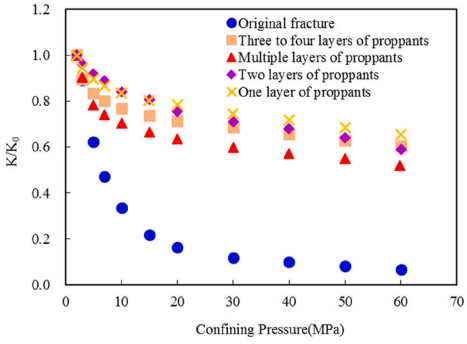

(d) The permeability ratio of propped fracture with different numbers of layers of proppant for the third loading cycle.

Fig. 5. The permeability and permeability ratio of propped fractures with different numbers of layers of proppant for the third loading cycle.

Table 3
The fracture volume and porosity for different scenarios.

Sample ID	Without proppants	One layer of proppants	Two layers of proppants	Three to four layers of proppants	Multiple layers of proppants
Proppant weight (g)	0	3.30	4.99	7.50	14.07
Fracture volume (mm^3)	/	2934.9	4428	5148	12688
Porosity (%)	/	57.6	57.5	45.0	58.1

sand, kg/m^3; and V_F is the volume of the fracture, m^3.

The transient method, developed by Brace et al. (1968), is used to measure the permeability of the proppant following the schematic diagram of Fig. 1. The triaxial pressure chamber and stress loading sections of the system have been previously described (Chen et al., 2015b, 2018, 2018). This system is augmented by two Keller pressure sensors to monitor gas pressure in the upstream and downstream gas injection system. These sensors have a measuring range and accuracy of 0–20 MPa and 0.05 % full scale, respectively. One Keller differential pressure transducer was installed between the upstream gas injection system and the downstream gas injection system. The measuring range and accuracy of the differential pressure transducer are 0–1 MPa and 0.1 % full scale, respectively (Chen et al., 2019). Gas was injected into the upstream and downstream gas system, and the gas pressure adjusted to establish the pressure difference between the upstream and downstream gas system (Chen et al., 2015b).

The pressure decay exponent, α, is proposed to measure the downtrend and defined as (Brace et al., 1968; Ma et al., 2016; Tan et al., 2017):

$$\frac{(P_u - P_d)}{(P_{u,0} - P_{d,0})} = e^{-\alpha t} \tag{2}$$

where P_u (MPa) and P_d (MPa) are the pressure of the upstream reservoir and the downstream reservoir at time t during permeability measurement, respectively. $P_{u,0}$ (MPa) and $P_{d,0}$ (MPa) are the pressure of the upstream gas system and the downstream gas system at the initial time of permeability measurement, respectively. The measured permeability k can be expressed in terms of pressure decay exponent, α, as (Brace et al., 1968; Tan et al., 2018):

$$k = 2\mu L\alpha \Big/ \left(\frac{A(P_{u,0} + P_{d,0})}{2\mu L}\left(\frac{1}{V_u} + \frac{1}{V_d}\right)\right) \tag{3}$$

where k is the permeability, m^2; A is the cross-sectional area of the sample or the fracture with proppants, m^2; L is the length of the sample, m; μ is the viscosity of the fluid flowing through the sample, Pa·s; and V_u (m^3) and V_d (m^3) are the volumes of the upstream gas system and the downstream gas system, respectively. During the measurement, the volumes of the upstream (V_u) and the downstream gas (V_d) systems are determined with impermeable stainless steel sample placed in the core holder. The gas injection system is firstly vacuumed and then the gas was injected from both upstream and downstream gas systems with two high precision metering pumps, respectively. When the gas volume in the injection pump remains constant, the equilibrium state is achieved and the volumes of upstream and downtown gas systems are obtained by the volume difference recorded before and after injection, respectively. In this work, the volumes of the upstream and downstream gas systems are the same.

The saturant is Helium and this is used in the permeability measurement in this work. To eliminate air contamination in the apparatus, the gas injection system and the shale sample were placed under a vacuum for at least 72h after installation of the sample (Wang et al., 2016).

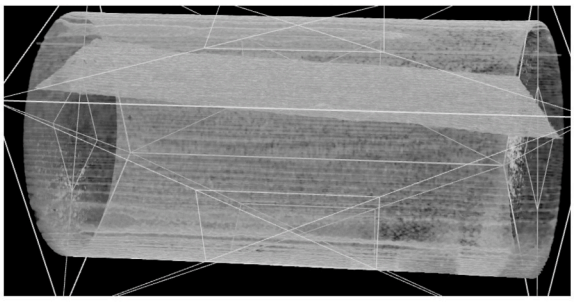

(a) Proppants in the shale sample.

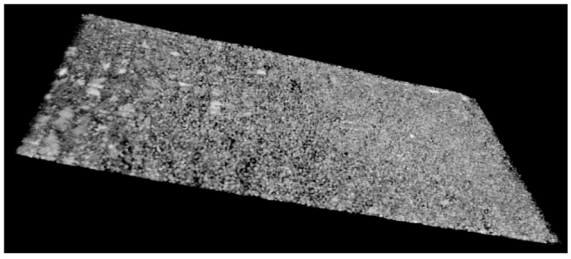

(b) Proppant distribution in the natural fracture.

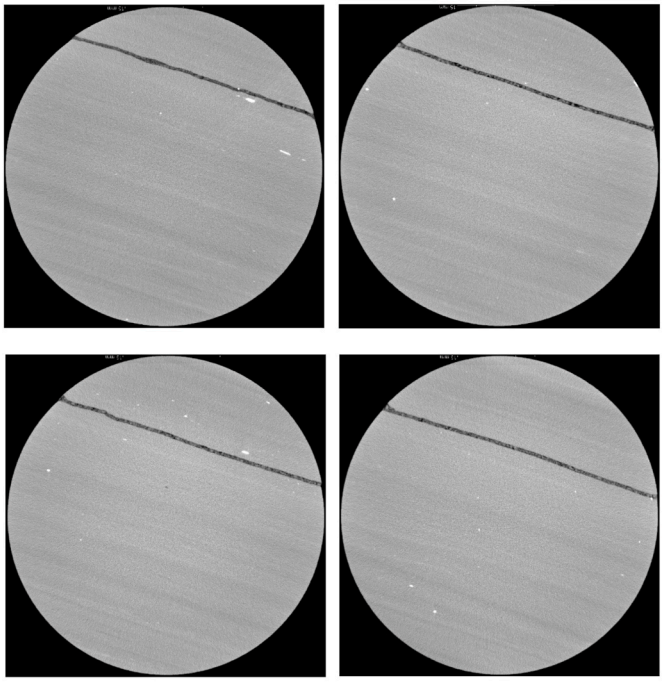

(c) Proppant distribution in 1/5, 2/5, 3/5 and 4/5 of horizontal cross sections of the

Fig. 6. The distribution of one layer of proppant in the fracture following permeability measurement.

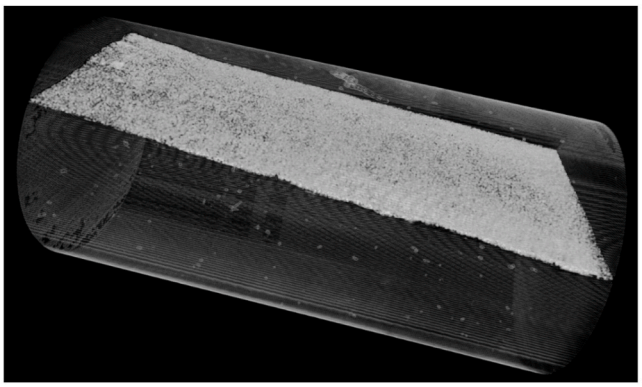

(a) Proppant in the shale sample.

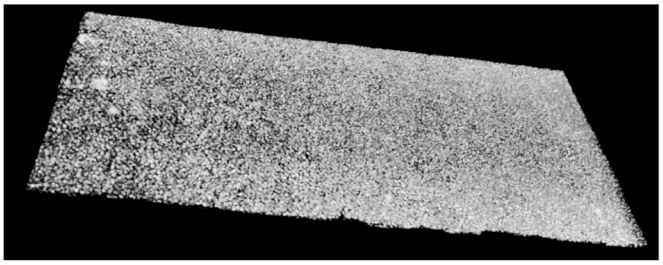

(b) Proppant distribution.

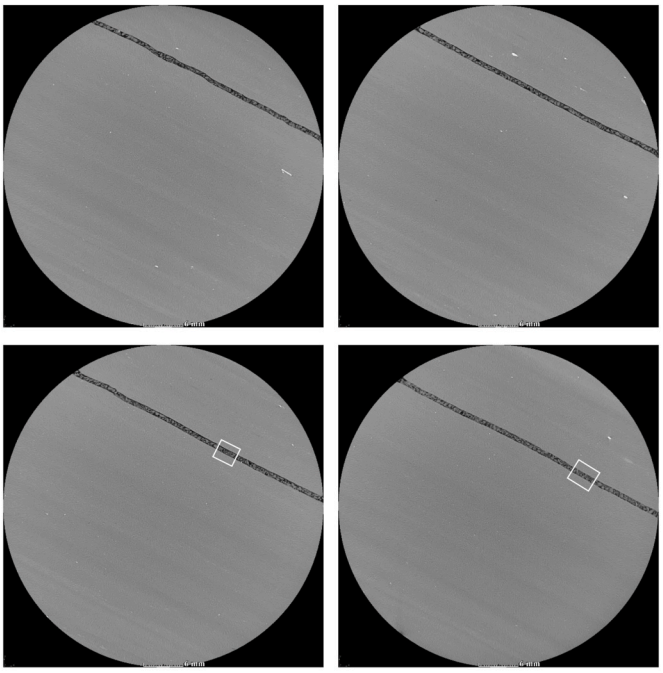

(c) Proppant distribution in 1/5, 2/5, 3/5 and 4/5 of horizontal cross sections of the sample (left to right and top-bottom)

Fig. 7. The distribution of two layers of proppant in the fracture following permeability measurement.

Then hydrostatic confining pressure was applied to the sample with a loading rate of 1 MPa/min. Effective stress was incremented in the permeability experiments from 1.5 MPa to 59.5 MPa using ten confining pressure steps. The value of 1.5 MPa corresponds to the gas full saturation state (initial state) with the value of 59.5 MPa to the gas complete depletion state (Cui et al., 2020a). In this study, the effective stress is defined as the difference between the confining pressure and gas pressure. When the permeability measurement in the first loading process was completed, the effective stress was reduced to 1.5 MPa and the permeability was measured following the reversed confining pressure steps. In order to consolidate the sample, after the permeability measurement of the first loading and unloading process, the permeability measurement of the shale sample was repeated twice following the same loading and unloading path (Wang et al., 2014, 2021). All permeability tests were performed at 30 °C to guarantee the accuracy of experiment results.

The equivalent permeability of the shale sample with the original fracture but without proppant was first measured as the baseline and the cross-sectional area of the core sample is specified to the value of A in Eq. (4). Then, five scenarios with different multi-layer thicknesses were studied in succession to investigate the effect of proppant layer number/

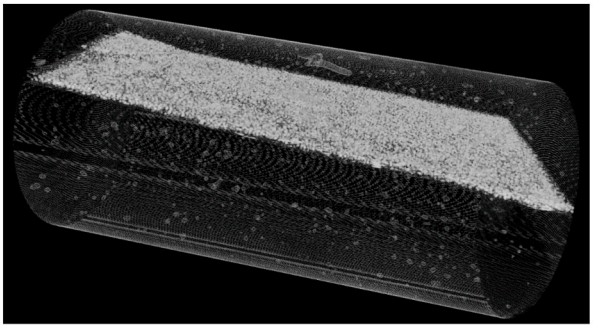

(a) Proppant in the shale sample.

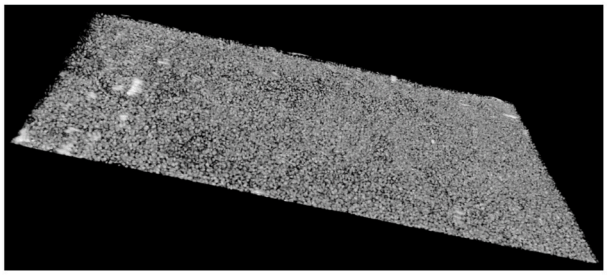

(b) Proppant distribution.

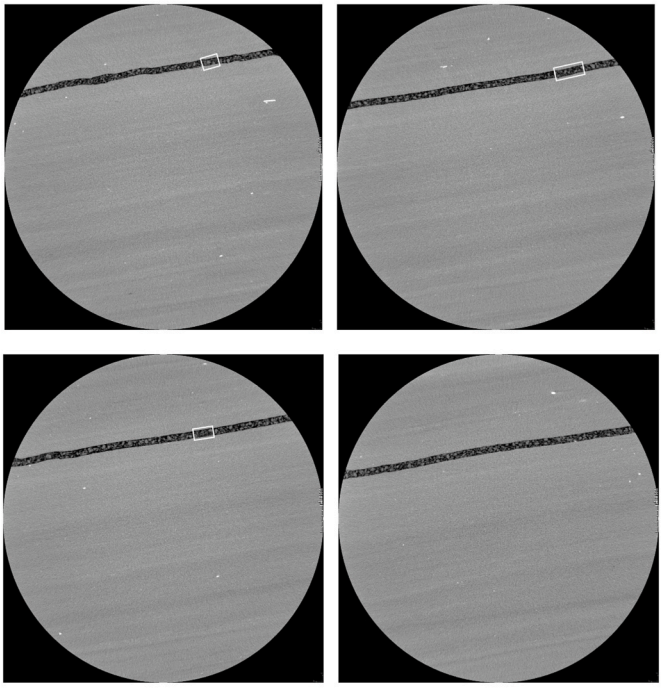

(c) Proppant distribution in 1/5, 2/5, 3/5 and 4/5 of horizontal cross sections of the sample (left to right and top-bottom).

Fig. 8. The distribution of three to four layers of proppants in the fracture following permeability measurement.

thickness on shale fracture permeability. The five scenarios were with a none, monolayer and then with two-, three-then four-layers, and finally with multiple layers of proppant, respectively. Fig. 2 shows the shale sample for the different scenarios. For the case with triple/quadruple layers of proppant, the end face filled with dry sand was the other end face of the original sample shown in Fig. 2(d), so the final photographed end face was different from that of the other cases. However, no matter which end face was used for more dry sand particle filling, the shale fracture was completely filled with sand particles in these different cases.

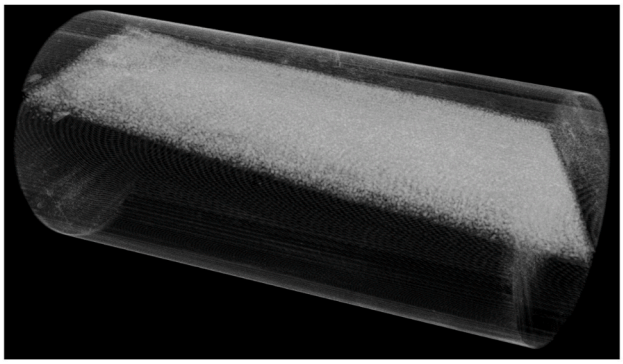

(a) Proppant in the shale sample.

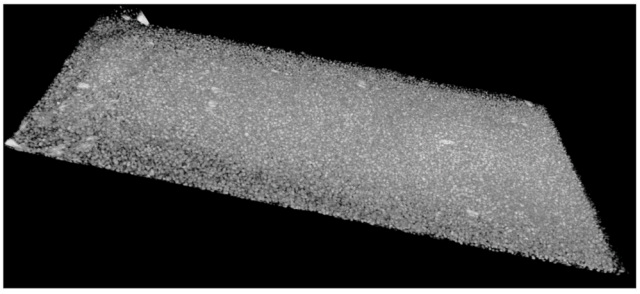

(b) Proppant distribution.

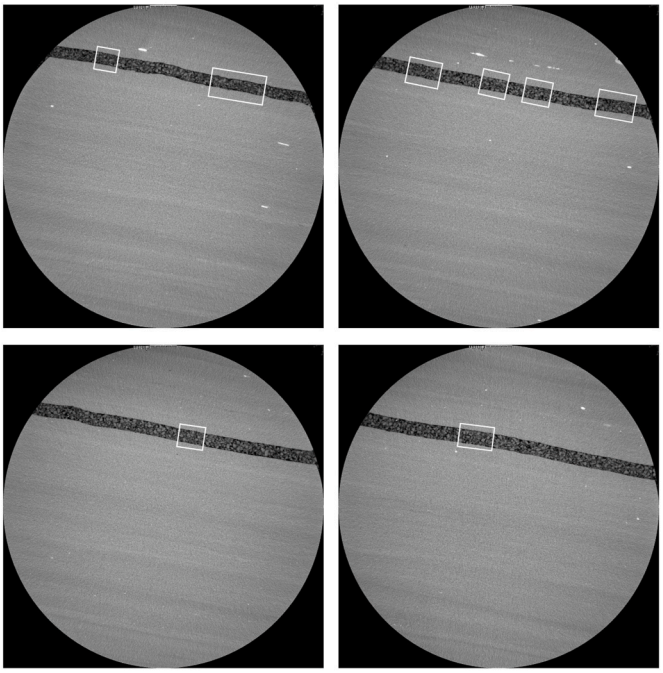

(c) Proppant distribution in 1/5, 2/5, 3/5 and 4/5 of horizontal cross sections of the sample (left to right and top-bottom).

Fig. 9. The distribution of multiple layers of proppants in the fracture following permeability measurement.

After each permeability test (one per scenario) was completed, the shale sample was removed from the pressure chamber with the thermal-shrink-wrap sleeve intact and scanned by X-ray CT using a nanoVoxel 4000 industrial scanner. Then the fracture was opened, the proppant distribution and performance, and the interaction between proppant particles and fracture surface on the fracture surface observed by optical microscopy. Finally, the proppant particles were removed from the fracture and the proppant particle size distribution was determined by

Table 4
The modeling parameters using Eq. (4).

		Run 1-decreasing p_c	Run 2-increasing p_c	Run 2-decreasing p_c	Run 3-increasing p_c	Run 3-decreasing p_c	Run 4-increasing p_c	Run 4-decreasing p_c
Case 1	k_0 (mD)	0.043	0.067	0.039	0.059	0.047		
	C_f (MPa^{-1})	0.0081	0.0097	0.0087	0.011	0.011		
	AAD%	28.41	26.43	29.11	28.17	28.86		
Case 2	k_0 (mD)	2.55	2.72	2.05	2.17	1.86		
	C_f (MPa^{-1})	0.0013	0.0025	0.0011	0.0018	0.0011		
	AAD%	4.23	2.54	4.15	2.86	4.10		
Case 3	k_0 (mD)	3.85	4.18	3.23	3.35	2.95	3.10	2.73
	C_f (MPa^{-1})	0.0015	0.0026	0.0013	0.0019	0.0014	0.0018	0.0012
	AAD%	4.63	3.08	4.60	3.39	4.54	3.02	4.19
Case 4	k_0 (mD)	2.41	2.65	2.08	2.18	1.89		
	C_f (MPa^{-1})	0.0016	0.0025	0.0013	0.0019	0.0012		
	AAD%	6.17	4.32	5.50	4.12	5.03		
Case 5	k_0 (mD)	3.81	4.12	3.18	3.53	2.94		
	C_f (MPa^{-1})	0.0018	0.0028	0.0015	0.0026	0.0015		
	AAD%	6.47	5.53	7.59	6.21	7.15		

Table 5
The modeling parameters using Eq. (6).

		Run 1-decreasing p_c	Run 2-increasing p_c	Run 2-decreasing p_c	Run 3-increasing p_c	Run 3-decreasing p_c	Run 4-increasing p_c	Run 4-decreasing p_c
Case 1	k_0 (mD)	0.202	0.242	0.222	0.220	0.213		
	C_{f0} (MPa^{-1})	0.081	0.060	0.103	0.064	0.103		
	α	0.093	0.063	0.110	0.067	0.108		
	AAD%	7.24	4.50	5.99	3.83	6.46		
Case 2	k_0 (mD)	3.053	2.898	2.373	2.400	2.384		
	C_{f0} (MPa^{-1})	0.016	0.005	0.011	0.007	0.023		
	α	0.145	0.030	0.111	0.052	0.171		
	AAD%	1.07	1.50	1.21	1.86	1.76		
Case 3	k_0 (mD)	4.628	4.501	4.106	3.824	3.759	3.392	3.138
	C_{f0} (MPa^{-1})	0.014	0.007	0.022	0.009	0.022	0.006	0.010
	α	0.109	0.037	0.156	0.069	0.155	0.050	0.096
	AAD%	1.12	1.46	1.56	2.20	1.68	1.94	1.40
Case 4	k_0 (mD)	2.963	2.873	2.514	2.521	2.293		
	C_{f0} (MPa^{-1})	0.017	0.007	0.016	0.011	0.015		
	α	0.127	0.039	0.127	0.074	0.124		
	AAD%	1.61	2.18	1.56	2.61	1.85		
Case 5	k_0 (mD)	5.085	4.640	4.527	4.222	4.145		
	C_{f0} (MPa^{-1})	0.022	0.009	0.024	0.012	0.025		
	α	0.121	0.045	0.130	0.065	0.136		
	AAD%	2.53	3.36	2.20	3.34	2.44		

laser classifier.

3. Results

The following explores changes in propped-fracture permeability with effective stress for different proppant contents and during both loading and unloading cycles. CT scanning is used to define proppant particle distribution within the fracture for different scenarios following the measurement of permeability.

3.1. Sample permeability and CT results

It should be noted that the permeability refers to the equivalent permeability of the fractured core in this paper, except that in Section 4.5, it refers to the permeability of the fracture with the proppant pack. In the former term the cross-sectional area of the core sample is specified to cross-sectional area (A) in Eq. (4) with cross-sectional area of the proppant pack specified in the later term. The equivalent permeabilities of the fractured core for different scenarios during loading and unloading cycles are shown in Fig. 3. The first, second, and third loading cycle in this study correspond to the first, second, and third loading process in the experiment procedure. Consistently, the first, second, and third unloading cycle refer to the first, second, and third unloading process. The equivalent permeabilities of the fractured core exhibits hysteresis in this response which decreases with the increase of loading cycles. The permeability measured during the third loading cycle are used in this section since the proppant pack are sufficiently consolidated after the stress application. When the effective stress is increased from 1.5 MPa to 59.5 MPa, the permeability of all cases decrease with the effective stress. This is most extreme for the unpropped fracture (from 0.17 to 0.01 mD) and successively less severe for single- (2.20–1.58 mD), double- (3.46–2.42 mD), triple/quadruple- (2.38–1.58 mD), then multi-

Table 6
The modeling parameters using Eq. (8).

		Run 1-decreasing p_c	Run 2-increasing p_c	Run 2-decreasing p_c	Run 3-increasing p_c	Run 3-decreasing p_c	Run 4-increasing p_c	Run 4-decreasing p_c
Case 1	k_0 (mD)	0.255	0.490	0.315	0.452	0.274		
	β	0.798	0.775	0.796	0.765	0.796		
	C_k (MPa^{-1})	1.248	1.345	1.860	1.213	1.632		
	AAD%	12.11	4.53	10.01	5.70	10.11		
Case 2	k_0 (mD)	3.126	3.734	2.612	2.957	2.317		
	β	0.974	0.961	0.975	0.966	0.976		
	C_k (MPa^{-1})	2.619	3.152	3.920	3.989	3.917		
	AAD%	1.57	1.44	1.44	1.08	1.44		
Case 3	k_0 (mD)	5.236	6.161	4.294	4.835	3.959	4.312	3.573
	β	0.969	0.957	0.971	0.963	0.970	0.965	0.973
	C_k (MPa^{-1})	4.927	4.327	4.792	4.938	5.043	4.563	5.186
	AAD%	1.30	1.72	1.47	0.95	1.33	1.39	1.26
Case 4	k_0 (mD)	3.105	3.735	2.590	2.906	2.326		
	β	0.966	0.952	0.971	0.961	0.972		
	C_k (MPa^{-1})	2.093	1.987	2.035	1.992	1.978		
	AAD%	2.73	1.08	2.56	1.31	2.18		
Case 5	k_0 (mD)	5.233	6.399	4.621	5.162	4.081		
	β	0.958	0.941	0.956	0.949	0.962		
	C_k (MPa^{-1})	1.887	1.861	1.962	2.088	2.295		
	AAD%	2.92	1.62	3.55	1.91	3.37		

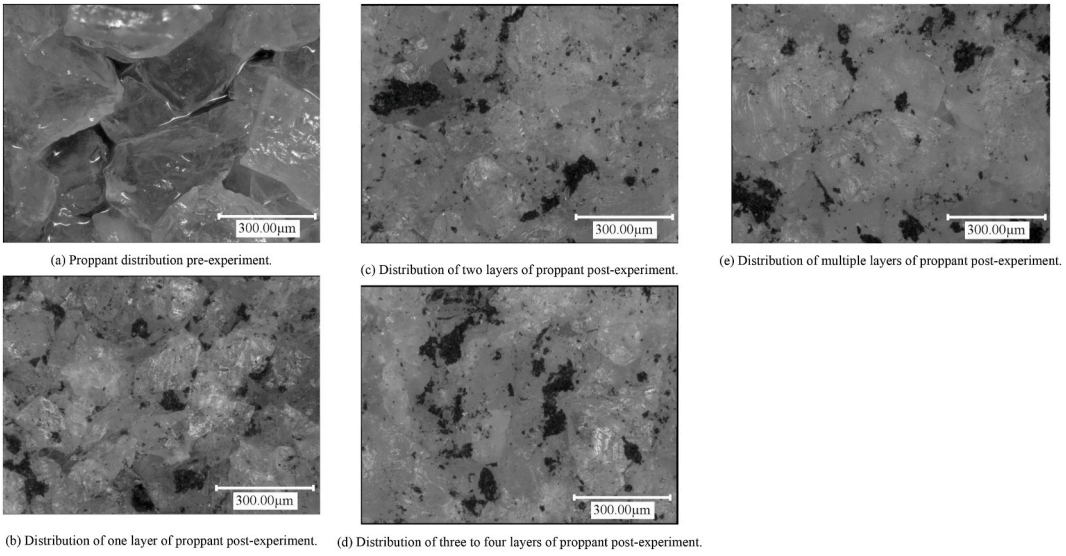

(a) Proppant distribution pre-experiment.
(b) Distribution of one layer of proppant post-experiment.
(c) Distribution of two layers of proppant post-experiment.
(d) Distribution of three to four layers of proppant post-experiment.
(e) Distribution of multiple layers of proppant post-experiment.

Fig. 10. Proppant pack both before and after the permeability experiments.

layers (4.14–2.36 mD) of proppant. The equivalent permeabilities of the core with original fracture decrease by two orders of magnitude with those of the proppant supported fractures changing progressively much less as the number of layers increases. The equivalent permeabilities of the core with proppant supported fractures are between one and two orders of magnitude higher than that of original fracture effective stresses of 1.5 MPa and 59.5 MPa, respectively.

The permeability ratio (k/k_0) is calculated to compare the downtrend of different cases. The value of k_0 refers to the value at the first confining pressure step (2 MPa) under the same experimental conditions (proppant layer). The permeability ratio of the shale core with fracture alone and filled with different layer thicknesses of proppant are shown in Fig. 4. As shown in the figure, the permeability ratio of cases without proppant declines faster than cases with proppant. While no universal rule is found when comparing the cases of different proppant layer.

Also in order to visually compare the effects of the number of proppant layers on the equivalent permeability of the fractured core, the permeabilities for the final loading cycle are summarized in Fig. 5. When the effective stress increases from 1.5 MPa to 59.5 MPa, the permeability ratio at the end of loading step for the third loading cycle shows the greatest sensitivity (reduction) for the unpropped fracture (0.066) with less sensitivity for 1-, 2-, 3/4- and multi-layers (at 0.65, 0.59, 0.61 and 0.52). Permeability ratio for the propped fracture with multi-layered proppant is surprisingly the lowest among the four cases with proppants. Also observed in Fig. 5, the permeability of the fractured core with multiple layers of proppant does not dramatically increase, compared to that with a single layer of proppant. The equivalent permeability for the fractured core at low stress (1.5 MPa) with multi-layered proppant is 2.1, 1.3, and 1.9 times higher than that with 1-, 2- and 3/4-layers of proppant, respectively. Likewise, it is 1.5, 1.0, and 1.5 times higher than that with 1-, 2- and 3/4-layers of proppant, respectively at an effective stress of 59.5 MPa, respectively.

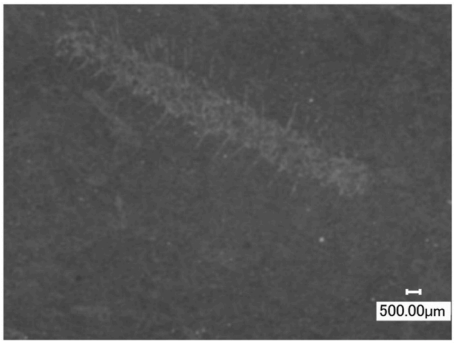

(a) Fracture surface before experiments.

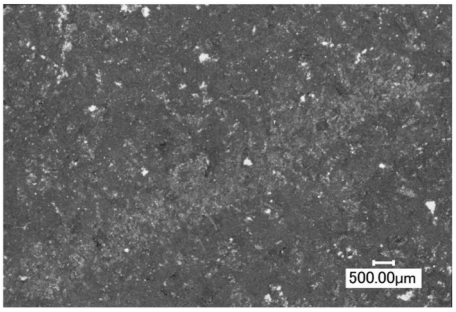

(b) Fracture surface after the permeability experiments.

Fig. 11. Embedment of proppant.

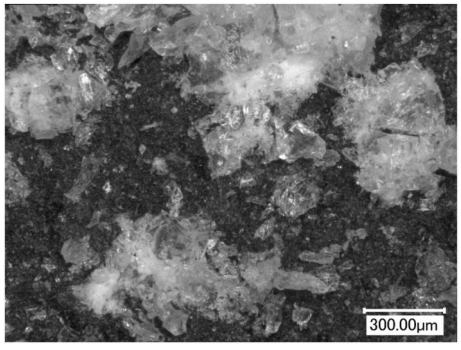

Fig. 12. Proppant crushing.

The proppant weight, fracture volume and the porosity of the proppant pack before the experiments for the five cases (0-, 1-, 2-, 3/4-, multi-) are shown in Table 3. Before the experiment, the porosity of the proppant pack for the four scenarios ranges from 45.0 % to 58.1 %. The proppant pack is compacted after the experiments, and it is transformed from a loose medium into a medium with a certain adhesion between the sand particles. Large vacancies among proppants may cause anomalies in permeability. The distribution of different layers of proppants in the fracture obtained by X-ray CT imaging post-experiment are shown in Figs. 6–9. In each figure, the CT images of four horizontal cross sections located at 1/5, 2/5, 3/5 and 4/5 of the sample are drawn. These images combined with original figures illustrate that (1) the proppants would be crushed and tensely compacted under the high effective stress as shown in the white boxed in Figs. 6–9; (2) the compaction would changes the topological structure of proppant pack blocking the flow channel and reducing the permeability; and (3) the compaction behavior are commonly observed in cases of multi-layer proppants and while in the case of one layer proppant little compaction would be detected.

3.2. Sample compressibility results

The relationship between permeability and stress for fractured reservoirs is widely assumed to be exponential (McKee et al., 1988):

$$k = k_0 e^{-3C_f(\sigma-\sigma_0)} \tag{4}$$

where k is the permeability at effective stress σ (MPa), k_0 (μm^2) is initial permeability at initial effective stress and σ_0 (MPa) and C_f (MPa^{-1}) is the compressibility of the fracture or interstitial proppant (Dong et al., 2010; Mitra et al., 2012; Tan et al., 2018; Zheng et al., 2012).

To study the relationship between the equivalent permeability for the fractured core and effective stress, and to obtain the equivalent compressibility of the fracture for the five different scenarios, all experimental data of permeability and effective stress were fitted to Eq. (4). In this, the initial effective stress σ_0 is assumed to be 0 MPa. The model parameters and average absolute deviation percentage (AAD%) are shown in Table 4. To make the comparison more meaningful, the fitting results of the first pressurization cycle are excluded from Table 4, as the sample was not consolidated. The permeability results obtained by model fitting are also shown in Fig. 5(a). Because the fitting of permeabilities for different loading cycles are similar, only the modeling results of the third loading cycle are selected. As can be seen from Table 4 and Fig. 5(a), the fitting results of the model deviate from the experimental data, indicating the inadequacy of the model – potentially resulting from a nonlinear fracture compressibility over the large range in effective stress (Dong et al., 2010; Tan et al., 2019).

In Eq. (4), the compressibility is constant resulting in a significant deviation between the model and the experimental data. Fracture compressibility is typically stress-dependent when the range of effective stress change is large (Chen et al., 2015a). Thus, the exponential relationship between permeability and stress is used to fit the experimental data with two different stress-dependent fracture compressibility models (Li et al., 2013; McKee et al., 1988; Shi and Durucan, 2010; Tan et al., 2017).

McKee et al. (1988) assumed an empirical fracture compressibility which exponentially decreases with increasing effective stress and introduced a mean compressibility $\overline{C_f}$ to replace C_f in Eq. (4):

$$\overline{C_f} = \frac{C_{f0}}{\alpha'(\sigma-\sigma_0)}\left(1-e^{-\alpha'(\sigma-\sigma_0)}\right) \tag{5}$$

where $\overline{C_f}$ is the average compressibility over the stress interval $\sigma - \sigma_0$; C_{f0} is the compressibility at an initial effective stress σ_0; and α' is the rate of decline of pore compressibility as effective stress increases.

Applying Eq. (5) into Eq. (4), yields:

$$k = k_0 e^{-3\frac{C_{f0}}{\alpha'(\sigma-\sigma_0)}\left(1-e^{-\alpha'(\sigma-\sigma_0)}\right)(\sigma-\sigma_0)} \tag{6}$$

Li et al. (2013) proposed a mean fracture compressibility based on the assumption made by Liu and Rutqvist (2009), considering that the fracture aperture has two parts: a residual component which is not compressible and a stress-dependent component. The mean fracture compressibility is derived as (Li et al., 2013):

$$\overline{C_f} = \frac{a}{\sigma-\sigma_0}\ln\left(\frac{\sigma+b}{\sigma_0+b}\right) \tag{7}$$

where a and b are modeling parameters.

Substituting C_f in Eq. (1) with $\overline{C_f}$ in Eq. (7), yields:

$$k = k_0 e^{-3\frac{a}{\sigma-\sigma_0}\ln\left(\frac{\sigma+b}{\sigma_0+b}\right)(\sigma-\sigma_0)} \tag{8}$$

The modeling results using Eq. (6) are shown in Fig. 5(b) and the model parameters are listed in Table 5, and those using Eq. (8) are shown in Fig. 5(c) and listed in Table 6, respectively. It can be seen from the modeling results that both models can well describe the

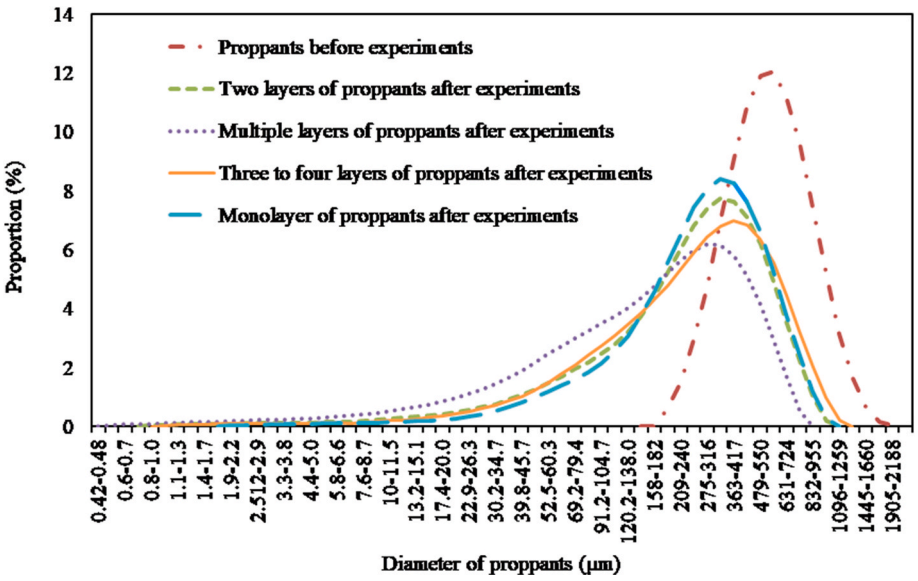

(a) Particle size distributions of the proppant both pre- and post-loading.

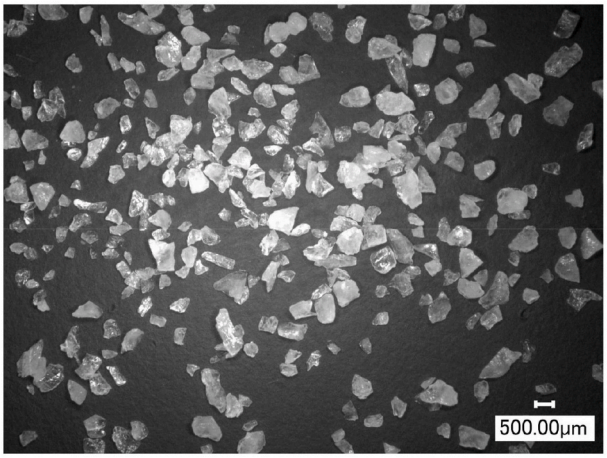

(b) Native proppants.

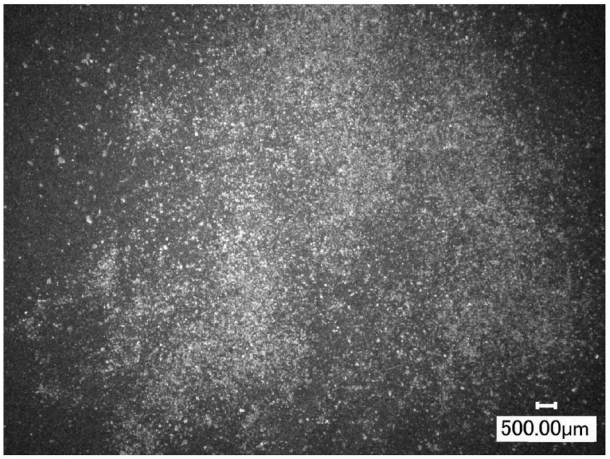

(c) Proppant post-experiment.

Fig. 13. Optical images and size variation of proppants after the permeability experiments.

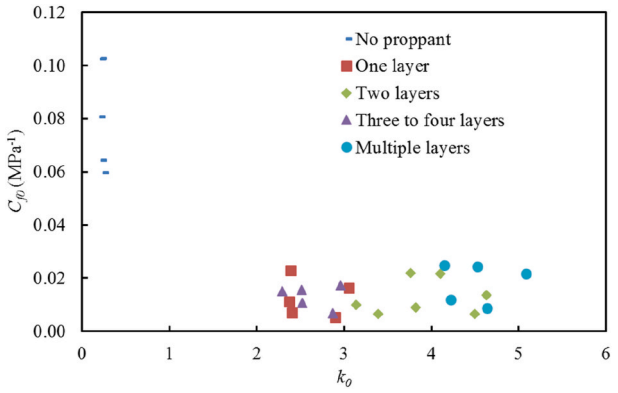

Fig. 14. The relationship between C_{f0} and k_0 using Eq. (6).

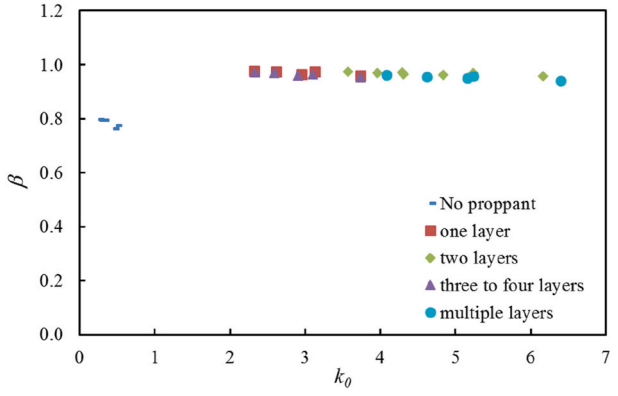

Fig. 15. The relationship between β and k_0 using Eq. (8).

experimental data.

4. Discussion

Given the non-constant compliance of the fracture, we investigate the relationship between the permeability of both un-propped and propped shale fractures under changes in effective stress.

4.1. Proppants topological structure changes

4.1.1. Proppant distribution

Fig. 10(a) illustrates the proppant distribution over the fracture surface before the permeability experiments with those post-testing experiments illustrated in Fig. 10(b)–(e). Before experiment, the configuration of each proppant is clearly distinguished which can be determined by naked eye. After experiment, the proppant also exhibit clearly boundaries in the case of one proppant layer but the spaces between different proppant particles are compacted (Fig. 10(b)); After compaction, the topological structure of proppant is damaged and the proppant particles are cohered especially for the cases of more than two-layer proppants. More crushes of proppant and compaction between particles would be observed in the cases of multi-layer proppants. This phenomenon is consistent with the foundlings in Figs. 6–9(c). Also, shale mineral fragments are shown to break from the fracture surface and adhere to the proppant pack post experiment. The fine particles generated by proppant crushing and also sourced from the fracture face may be mobilized by the gas flow and migrate into the pores and plug active flow channels - potentially reducing the conductivity of the fracture.

The fossilized graptolite has a sharp outline on the fracture surface before the experiments as shown in Fig. 11 (a). However, after the experiments, the outline of the graptolite was successively blurred, indicating damage that has resulted from friction and compression between the proppant particles and the fracture surface under the action of stress (Fig. 11 (b)). Nevertheless, this damage is inconsequential in modifying the roughness of the same sample, therefore has little impact for the sample to be used in subsequent experiments. Following the permeability experiments, the fracture surface was cleaned by a compressed air jet (pressure of 0.8 MPa) before the fracture surface was observed. However, residual proppant particles on the fracture surface can still be observed in Fig. 11 (b), which suggests that the proppant particles have firmly embedded into the fracture surface under the high stress. The proppant morphology on the fracture surface following the experiments is shown in Fig. 12. As shown in both Fig. 10 (a) and 12, the proppant particles break into small and irregular fragments due to the action of high stress. Compression, crushing and embedment of the proppant can lead to a reduction in fracture width, resulting in a corresponding reduction and hysteresis of the permeability.

4.1.2. Proppant size variation

The proppant and their size variation both before and after the permeability experiments are shown in Fig. 13. It should be noted that the proppant particle size distribution may entrain some induced fragments from the crushing of the fracture surface. It can be seen from Fig. 13 (a) that the pre-experiment proppant PSD ranges from 158 μm to 2188 μm. After the permeability experiments, 23.9 %, 26 %, 30 % and 41 % of the proppant particles are smaller than 158 μm for 1-, 2-, 3/4- and multi-layered particles, respectively. When the applied stress is above 20 MPa, the crushing of quartz sand increased significantly with increasing stress (Hampton et al., 2015). Particles as small as 1 μm can be detected after the experiments. This indicates the significant role of crushing under high stress. The proportion of newly-formed finer crushed particles increases with the number of proppant layers, suggesting that the crushing between the proppants are more significant perhaps due to the stress concentration among the irregular shaped particles. It should be noted that the influence of the number of proppant layer on packing permeability is different from the conclusion of the study of Elsarawy and Nasr-El-Din (2018). The size of sand grains used in the study of Elsarawy and Nasr-El-Din is 20/40 mesh and that used in our study is 30/50 mesh. It was demonstrated that the sand grain crushing force increased with increasing size (Brzesowsky et al., 2011). Different proppant sizes may result in different mechanical behaviors of proppants under the same stress conditions. In addition, the difference of fracture roughness and angle may be one of the reasons for the different results of the two studies. The proportions of post-experiment proppant particles larger than 955 μm in diameter decreases by 10.6 %, 9.6 %, and 10.9 % for proppant packs with 1-, 2-, and multi-layers, respectively. It can be observed from Fig. 13 (b) and 13 (c) that the native proppants are finely crushed during the experiments. The fine particles generated by proppant crushing and also sourced from the fracture face may be mobilized by the gas flow and migrate into the pores and plug active flow channels - potentially reducing the conductivity of the fracture.

4.1.3. Relationship between proppant redistribution and permeability

Following compaction in the first loading cycle, the equivalent permeability of the fractured core with proppants for the loading cycle was, surprisingly, higher than that for the unloading cycle as stresses were reduced. The unusual situation may be related to the rearrangement of proppant fragments and the transport and clogging of crushed fine proppant (Herskovits et al., 2016; Mittal et al., 2017). At higher stresses, the permeability of the proppant-supported fractured core for the loading cycle is typically lower than that for the unloading cycle. This implies that as the number of stress cycles increases, high stress results in increased crushing and generation of fine particles from both proppant and the shale surface. This is consistent with the conclusion of Herskovits et al. (2016) that the proportion of proppant breakage increased with increasing of the stress cycles.

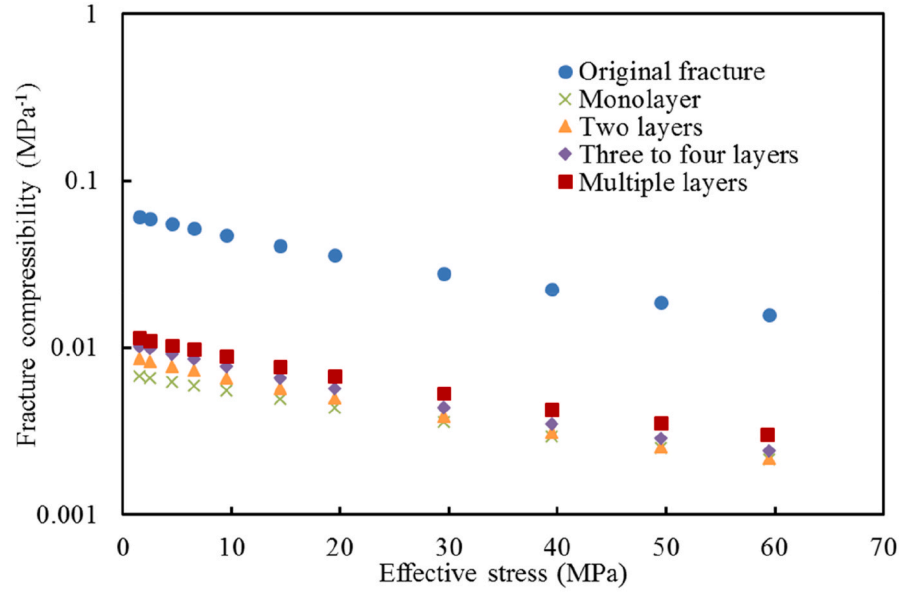

(a) Modeling results using Eq. (6).

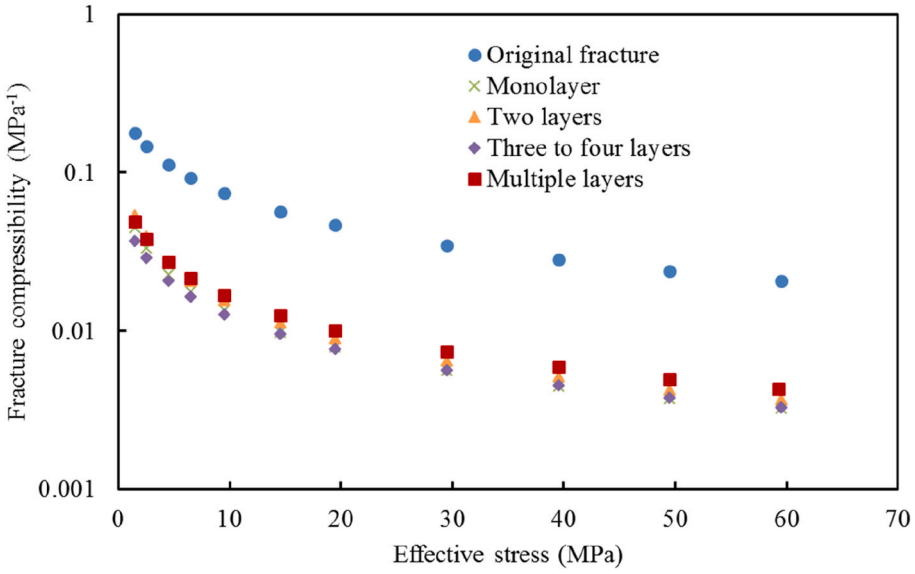

(b) Modeling results using Eq. (8).

Fig. 16. The relationship between mean fracture compressibility and effective stress using Eqs. (6) and (8).

4.2. *Permeability modeling*

In this section, the relationships between the modeling parameters for the different stress-dependent fracture compressibility models are discussed and the results are compared. Again, the first series of data (Run 1-increasing confining process), representing the seating-in cycle, are eliminated from the data set used in the modeling.

The relationship between C_{f0} and k_0 using Eq. (6) is plotted in Fig. 14. The C_{f0} for Case 1 (no proppant) range from 0.060 to 0.103 MPa^{-1} and from 0.005 to 0.025 MPa^{-1} the other scenarios (with layered proppant). The results indicate that fracture permeability is less sensitive to stress for fractures containing proppant which is consistent with the results from Tan et al. (2017) and Tan et al. (2019) – and results from the elastic modulus of proppants (81 GPa) (Valdes et al., 2017) being significantly higher than that of the shale (22 GPa) (Zuo et al., 2015).

The results in parameter inter-relationships between modeling parameters using Eq. (8) shown in Fig. 15. Here two new parameters are defined: $\beta = 1/(1+a)$ representing the ratio of the volume of the incompressible pore V_{IC} to the total pore volume V and $C_k = 1/\beta b$ denoting the compressibility for the compressible pore volume. Apparent from Fig. 15 that β (the ratio of the volume of the incompressible pore V_{IC} to the total pore volume V) is ~0.8 for Case 1 (no proppant), but ~1.0 for all other cases (with proppants). C_k (compressibility of the po、re volume) for Case 1 (un-propped) is

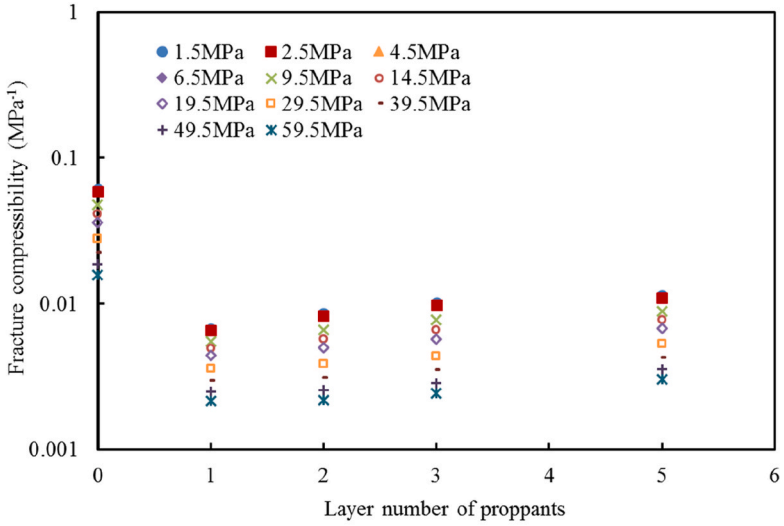

(a) The relationship between the mean fracture compressibility and the number of layers of proppant using Eq. (6).

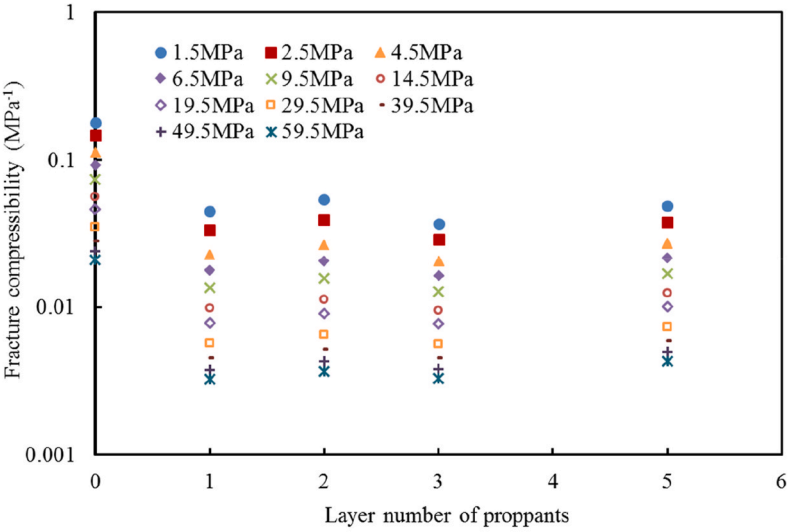

(b) The relationship between the mean fracture compressibility and the number of layers of proppant using Eq. (8).

Fig. 17. The relationship between the mean fracture compressibility and the number of layers of proppant using Eqs. (6) and (8).

1.213–1.860 MPa^{-1}, lower than that for the other cases (propped) which are 1.861–5.186 MPa^{-1}. The reason is that proppant increases the fracture aperture, leading to a greater pore volume and higher C_k.

4.3. *Fracture compressibility relationship with high stress*

The relationship between mean fracture compressibility and effective stress, using Eqs. (6) and (8) for the third loading cycle, are shown in Fig. 16. The compressibilities of the original fracture and propped fracture both decrease with an increase in effective stress. This indicates that the residual fracture opening decreases with an increase in effective stress, leading to a reduction in the fracture permeability. The compaction, crushing, and embedment of the proppant particle because of the increased effective stress results in a decrease in the porosity of the proppant pack, which further reduces the compressibility and permeability of the supported fracture (Bortolan Neto et al., 2015). The mean compressibilities of proppant-supported shale fracture are lower than that of the original fracture suggesting that the support of the proppants reduces the degree of fracture closure under stress conditions. The mean compressibilities of these two types of fractures decrease with increasing stresses.

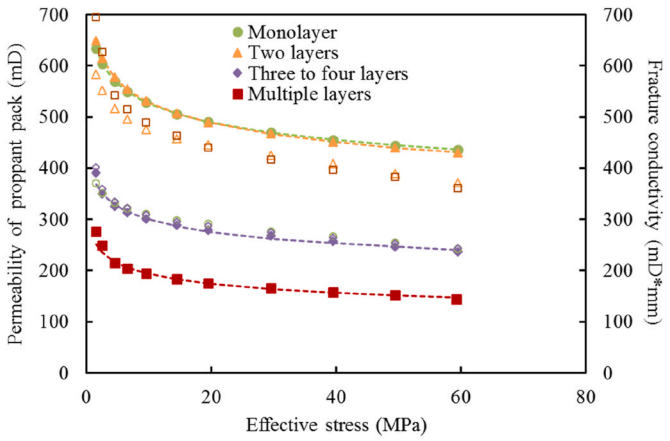

Fig. 18. Modeling results for the permeability of the proppant pack using Eq. (8) (solid symbol: permeability of proppant pack; empty symbol: fracture conductivity).

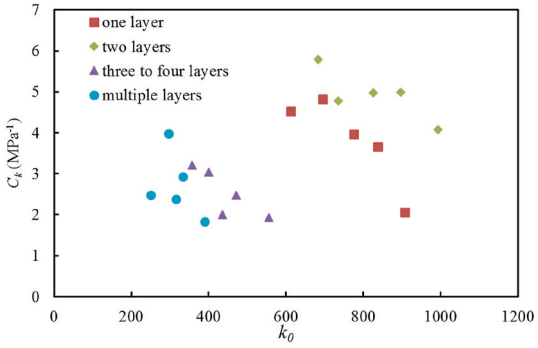

Fig. 19. The relationship between C_k and k_0 for the proppant pack using Eq. (8).

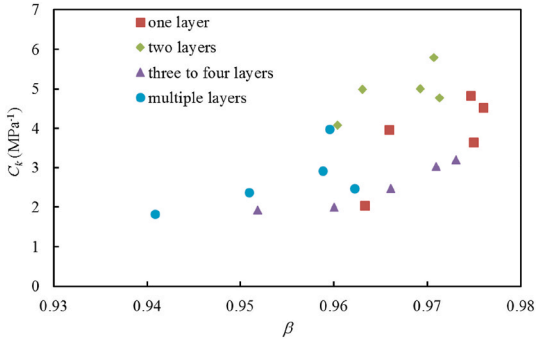

Fig. 20. The relationship between C_k and β of the proppant pack using Eq. (8).

4.4. Relationship between fracture compressibility and proppant layers

The number of proppant layers affect the permeability evolution of propped fractures. Apparent from Table 3, the porosity of the proppant pack was similar for both double layers and multiple layers of proppant within the fracture, and the permeability evolution of the two scenarios is similar. The triple to four layer proppant pack has the lowest porosity. This may be the reason that the permeability of the fracture with three or four layers of proppants is lower than that with two or multiple layers of proppants. Although the porosity of the mono-layer proppant pack is slightly higher, the reduced displacement degree-of-freedom of the proppant sandwiched between the fracture surfaces may result in the higher degree of proppant embedment under high stress (Zhang et al., 2017), resulting in lower compressibility and permeability of the propped fracture. It should be noted that the proppant may be realigned, aggregated and fragmented under stress, therefore, the layers may be altered. This may also affect the flow conductivity of proppant pack.

Fig. 17 shows the relationship between the mean fracture compressibility and the number of layers of proppant using Eqs. (6) and (8) for the third loading cycle of each case. It should be noted that the number of layers of proppants for different cases was simply determined according to the end face of the sample shown in Fig. 2. It can be seen from the figure that the mean fracture compressibility obtained from Eq. (6) tends to increase as the number of layers of proppant increases. The increase of the mean compressibility obtained from Eq. (8) with the number of layers of proppant is not significant. The mean fracture compressibilities with 1-, 2-, 3/4- and multi-layers of proppant using Eq. (6) are 0.00215, 0.00217, 0.00241, and 0.00302 MPa^{-1} at an effective stress of 59.5 MPa, respectively – and using Eq. (8) yields 0.00322, 0.00366, 0.00327, and 0.00429 MPa^{-1} at the same effective stress (59.5 MPa), respectively.

4.5. Permeability and compressibility of the proppant pack

The above analyses are all based on equivalent permeability of the sample with a proppant filled fracture. However, it would also be interesting to investigate the permeability and fracture compressibility for the proppant filled fracture itself for comparison among the different scenarios. Therefore, in this section, the permeabilities of the proppant pack for different scenarios are calculated separately using the average area and length of the propped fracture based on Eq. (2) and Eq. (3), and the compressibility of the proppant pack is also calculated using Eq. (8). The modeling results for the permeability of proppant pack using Eq. (8) are shown in Fig. 18. The permeability of the proppant pack decreases as proppant layer increases. The sand proppant is irregular in shape, and there are more contact points between the proppant particles in a multi-layer proppant pack and this is more prone to proppant failure under stress (Bolintineanu et al., 2017), resulting in more crushed fine particles in the multi-layer proppant pack (Fig. 13 (a)). This may be one of the reasons why the permeability of the proppant pack decreases with an increase in the number of layers. The trend of the fracture conductivity of the cases with different proppant layers in Fig. 18 is similar to that of the permeability for the sample with a proppant filled fracture in Fig. 5 (a). From Figs. 19 and 20, it can be concluded that C_k (compressibility of the compressible pore volume of the proppant pack) decreases with an

Table 7
The comparisons of modeling parameters using Eq. (4).

Sample with fracture	AAD%	Sample with proppants (one layer)	AAD%	Sample with proppants (two layers and above)	AAD%	Sample	
0.0011–0.0081	26.43–29.11	0.0011–0.0025 quartz	2.86–4.23	0.0012–0.0028, quartz	3.02–7.59	Shale	Our work
0.051, 0.078	8.54,6.79	0.0093,0.013 glass beads	0.77,1.21	0.0030,0.012 glass beads	2.31,2.58	Shale	Tan et al., 2018
		0.0051,0.0080 sand	2.09,3.35	0.0083,0.013 sand	2.49,4.54		
		0.028 sand	6.76	0.02 sand	5.44	Coal	Wu et al. (2018)

Table 8
The comparisons of modeling parameters using Eq. (6).

Sample with fracture		AAD%	Sample with fracture (one layer)		AAD%	Sample with fracture (two layers and above)		AAD%
C_f	a'		C_f	a'		C_f	a'	
0.005–0.016 He	0.030–0.171 He	4.5–7.24	0.006–0.022 He	0.037–0.156 He	1.07–1.86 He	0.007–0.025 He	0.039–0.136 He	1.12–3.34
0.058–0.098 CH_4	1e-7-0.094 CH4	2.1–25.7	0.074–0.078 CH4	0.24–0.32 CH4	1.52–4.35	0.11–0.99 CH4	0.058–0.51 CH4	3.53–5.56
0.061–0.24 He	0.014–0.29 He	4.1–4.43	0.11–0.16 He	0.16–0.25 He	1.3–4.35	0.11–0.55 He	0.052–0.61 He	3.37–8.18

In the first line, the date is collected from our work while in the rest lines the data is collected from Tan et al. (2017) with glass beads applied as proppants.

increase in k_0, and that this increases with β (the ratio of the volume of the incompressible pore V_{IC} to the total pore volume V of the proppant pack). Moreover, C_k of the proppant pack for Case 5 (multiple layers of proppant) and Case 4 (three to four layers of proppants) are lower than that for Case 3 (two layers of proppant) and Case 2 (one layer of proppant), indicating that the sensitivity of compressibility for the compressible pore volume of the proppant pack decreases with an increase in the number of layers of proppant.

4.6. Comparisons with other work

The results are compared with previous work to verify applicability of this work. The comparisons of fitting results (c_f) using Eq. (4) are first conducted as shown in Table 7. The c_f values obtained in our work is in the same range as that in Tan's work and Li's work while much smaller than that in the Wu's work. The sample difference may be the main reason as the coal sample is softer than the shale sample leading to larger compressibility value. Our results are also consistent with results obtained in other hard rock. Shekhawat and Pathak (2016) obtained mean compressibilities of a propped fracture for high strength sandstone as 0.0058 to 0.0051 MPa^{-1} (N_2) for effective stresses in the range 35–65 MPa. The AAD% value is also compared and found that the value in this work is larger than the other work especially for the case without proppant. This characteristic indicates that Eq. (4) may be not suitable for the reservoirs with high effective stress especially for the fracture without proppant supported.

The fitting results with Eq. (6) are further compared with results in Tan's work as shown in Table 8. The compressibility value obtained in this work is one order smaller than those in Tan's while the values of a' are in the same range as those in Tan's work. The AAD% of our work is smaller than that in Tan's work indicating the feasibility of Eq. (6) to the high effective stress.

5. Conclusions

This work has explored the permeability evolution of fractures both without (unpropped) and with proppant (propped with variable layer thicknesses) together with the behaviour of proppant under high stress. The effects of the thickness/number of the proppant layer/s on the fracture permeability in shale were also studied. The fracture compressibility was obtained using different permeability models. Moreover, the relationships among high stress, proppant layer thickness and the mean fracture compressibility were studied. The following conclusions can be drawn:

1. The permeability of the shale sample with a propped fracture is one or two orders of magnitude higher than that with the original fracture permeability for effective stresses ranging from 1.5 to 59.5 MPa. The decrease of permeability with increased stress is largest for unpropped fractures (permeability reduces by one order of magnitude), and less for propped fractures (a fraction of an order of magnitude). The reduction in the permeability with increased stress increases as the number of layers increases (Fig. 5). This reflects the more sensitivity of the proppant to crushing as the number of layers increases and the greater propensity of the proppant to crushing for more dense packing. Surprisingly, overall permeability of the proppant pack decreases with an increase in thickness of the enclosed proppant.
2. The initial compressibility of the proppant-supported fractures is lower than that for the unpropped fracture. The mean compressibility of propped fractures is approximately one order of magnitude lower than that of the unpropped fracture and increases with the number of proppant layers. This suggests that compressibility is dominated by the mismatched fracture when unpropped but that the proppant has a high skeletal stiffness and couples stresses strongly with the fracture wall. The implications of this deformability are that fracture permeability is less sensitive to stress where proppant is present in the fracture.
3. The mean compressibility of the non-propped and propped fracture is not constant and reduces with an increase in confining stress. This indicates that the residual fracture opening decreases with an increase in effective stress, leading to a reduction in the fracture permeability. The compaction, crushing, and embedment of the proppant particles, resulting from this increase in effective stress, results in a decrease in the porosity of the proppant pack, which further reduces the compressibility and permeability of the supported fracture.

Author statement

Tianyu Chen: Conceptualization, Methodology, Resources, Data curation, Writing – original draft; Yanji Fu: Resources, Formal analysis, Investigation, Data curation; Xia-Ting Feng: Project administration, Funding acquisition; Yuling Tan: Methodology, Investigation, Visualization; Guanglei Cui: Resources, Writing – original draft, Writing – review & editing; Derek Elsworth: Methodology, Writing – review & editing; Zhejun Pan: Conceptualization, Methodology, Writing – review & editing,

Declaration of competing interest

The authors declare that they have no known competing financial interests or personal relationships that could have appeared to influence the work reported in this paper.

Acknowledgment

Funding from the National Natural Science Foundation of China (Grant Nos. 51609038 and 12002081), the Fundamental Research Funds for the Central Universities (Grant No. N180104021, Grant No. N160104002) and the 111 Project (Grant No. B17009) is gratefully acknowledged.

Nomenclature

φ_p	is the porosity of the proppant-propped fracture
m_s	is the weight of the sand filling the fracture, kg
ρ_s	is the true density of the sand, kg/m^3
V_F	is the volume of the fracture, m^3
P_u	is the pressure of the upstream reservoir, MPa
P_d	is the pressure of the downstream reservoir, MPa
$P_{u,0}$	is the pressure of the upstream gas system at the initial time of permeability measurement, MPa
$P_{d,0}$	is the pressure of the downstream gas system at the initial time of permeability measurement, MPa
α	is the pressure decay exponent
k	is the permeability, μm^2
A	is the cross-sectional area of the sample, cm^2
L	is the length of the sample, cm
μ	is the viscosity of the fluid flowing through the sample, Pa·s
V_u	is the volume of the upstream gas system, m^2
V_d	is the volume of the downstream gas system, ml
σ	is effective stress, MPa
k_0	is initial permeability, μm^2
σ_0	is initial effective stress, MPa
C_f	is the variable compressibility of the fracture or interstitial proppant, MPa^{-1}
$\overline{C_f}$	is the average compressibility over the stress interval $\sigma - \sigma_0$, MPa^{-1}
C_{f0}	is the compressibility at an initial effective stress σ_0, MPa^{-1}
α	is the rate of decline of pore compressibility as effective stress increases
a and b	are modeling parameters
V_{IC}	is the volume of the incompressible pore, cm^3
V	is the total pore volume, cm^3
β	is the ratio of the volume of the incompressible pore to the total pore volume
C_k	is the compressibility for the compressible pore volume, MPa^{-1}

References

Alramahi, B., Sundberg, M.I., 2012. Proppant embedment and conductivity of hydraulic fractures in shales. In: 46th U.S. Rock Mechanics/Geomechanics Symposium. American Rock Mechanics Association, Chicago, Illinois.

Arshadi, M., Piri, M., Sayed, M., 2018. Proppant-packed fractures in shale gas reservoirs: an in-situ investigation of deformation, wettability, and multiphase flow effects. J. Nat. Gas Sci. Eng. 59, 387–405.

Bolintineanu, D.S., Rao, R.R., Lechman, J.B., Romero, J.A., Jove-Colon, C.F., Quintana, E.C., Bauer, S.J., Ingraham, M.D., 2017. Simulations of the effects of proppant placement on the conductivity and mechanical stability of hydraulic fractures. Int. J. Rock Mech. Min. Sci. 100, 188–198.

Bortolan Neto, L., Khanna, A., Kotousov, A., 2015. Conductivity and performance of hydraulic fractures partially filled with compressible proppant packs. Int. J. Rock Mech. Min. Sci. 74, 1–9.

Brace, W.F., Walsh, J.B., Frangos, W.T., 1968. Permeability of granite under high pressure. J. Geophys. Res73 (6), 2225–2236.

Brzesowsky, R.H., Spiers, C., Peach, C., Hangx, S., Spiers, C., 2011. Failure behavior of single sand grains. Theory versus experiment 116, 1–13.

Chen, D., Pan, Z., Ye, Z., 2015a. Dependence of gas shale fracture permeability on effective stress and reservoir pressure: model match and insights. Fuel 139, 383–392.

Chen, D., Ye, Z., Pan, Z., Zhou, Y., Zhang, J., 2017. A permeability model for the hydraulic fracture filled with proppant packs under combined effect of compaction and embedment. J. Petrol. Sci. Eng. 149, 428–435.

Chen, T., Feng, X.-T., Cui, G., Tan, Y., Pan, Z., 2019. Experimental study of permeability change of organic-rich gas shales under high effective stress. J. Nat. Gas Sci. Eng. 64, 1–14.

Chen, T., Feng, X.T., Pan, Z., 2015b. Experimental study of swelling of organic rich shale in methane. Int. J. Coal Geol. 150–151, 64–73.

Chen, T., Feng, X.T., Pan, Z., 2018. Experimental study on kinetic swelling of organic-rich shale in CO2 , CH4 and N2. J. Nat. Gas Sci. Eng. 55, 406–417.

Cooke Jr., C.E., 1973. Conductivity of fracture proppants in multiple layers. SPE J. 25 (9), 1101–1107.

Cui, G., Liu, J., Wei, M., Feng, X., Elsworth, D., 2018a. Evolution of permeability during the process of shale gas extraction. J. Nat. Gas Sci. Eng. 49, 94–109.

Cui, G., Liu, J., Wei, M., Shi, R., Elsworth, D., 2018b. Why shale permeability changes under variable effective stresses: new insights. Fuel 213, 55–71.

Cui, G., Tan, Y., Chen, T., Feng, X.-T., Elsworth, D., Pan, Z., Wang, C., 2020a. Multidomain two-phase flow model to study the impacts of hydraulic fracturing on shale gas production. Energy Fuel. 34 (4), 4273–4288.

Cui, G., Chen, T., Feng, X., Chen, Z., Elsworth, D., Yu, H., Zheng, X., Pan, Z., 2020b. Coupled multiscale-modeling of microwave-heating-induced fracturing in shales. Int. J. Rock Mech. Min. Sci. 136, 104520.

Cutler, R.A., Enniss, D.O., Jones, A.H., Swanson, S.R., 1985. Fracture conductivity comparison of ceramic proppants. SPE J. 25 (2), 157–170.

Dong, J.-J., Hsu, J.-Y., Wu, W.-J., Shimamoto, T., Hung, J.-H., Yeh, E.-C., Wu, Y.-H., Sone, H., 2010. Stress-dependence of the permeability and porosity of sandstone and shale from tcdp hole-A. Int. J. Rock Mech. Min. Sci. 47 (7), 1141–1157.

Dusterhoft, R., Nguyen, P., Conway, M., 2004. Maximizing effective proppant permeability under high-stress, high gas-rate conditions. In: SPE Annual Technical Conference and Exhibition. Society of Petroleum Engineers, Houston, Texas.

Elsarawy, A.M., Nasr-El-Din, H.A., 2018. Proppant performance in marcellus shale fractures under experimental in-situ stress conditions. In: SPE/IADC Middle East Drilling Technology Conference and Exhibition. UAE, Society of Petroleum Engineers, Abu Dhabi.

Fan, M., McClure, J., Han, Y., Li, Z., Chen, C., 2017. Interaction between proppant packing, reservoir depletion, and fluid flow in hydraulic fractures. In: Offshore Technology Conference. Houston, Texas, USA, Offshore Technology Conference.

Fredd, C.N., McConnell, S.B., Boney, C.L., England, K.W., 2000. Experimental study of hydraulic fracture conductivity demonstrates the benefits of using proppants. In: SPE Rocky Mountain Regional/Low-Permeability Reservoirs Symposium and Exhibition. Society of Petroleum Engineers, Denver, Colorado.

Fredd, C.N., McConnell, S.B., Boney, C.L., England, K.W., 2001. Experimental study of fracture conductivity for water-fracturing and conventional fracturing applications. SPE J. 6 (3), 288–298.

Hampton, J.C., Nguyen, P., O'Connell, P., Matzar, L., 2015. Acoustic emission monitoring elucidates proppant pack strength characteristics during crush testing. In: 49th US Rock Mechanics/Geomechanics Symposium. American Rock Mechanics Association.

Han, J., Wang, J.Y., 2014. Fracture conductivity decrease due to proppant deformation and crushing, a parametrical study. In: SPE Eastern Regional Meeting. Charleston. Society of Petroleum Engineers, WV, USA.

Herskovits, R., Fuss-Dezelic, T., Shi, J., Wilcox, C., Kaul, T., 2016. Sand and ceramic proppant performance in thin layer/monolayer conditions subjected to cyclic stress. In: SPE Eastern Regional Meeting. Canton, Ohio, USA, Society of Petroleum Engineers.

Hou, L., Elsworth, D., Geng, X., 2020. Swelling and embedment induced by sub- and super-critical-CO2 on the permeability of propped fractures in shale. Int. J. Coal Geol. 225, 103496.

Hou, T., Zhang, S., Ma, X., Shao, J., He, Y., Lv, X., Han, J., 2017. Experimental and theoretical study of fracture conductivity with heterogeneous proppant placement. J. Nat. Gas Sci. Eng. 37, 449–461.

Kassis, S., Sondergeld, C.H., 2010. Fracture permeability of gas shale: effect of roughness, fracture offset, proppant, and effective stress. In: International Oil and Gas Conference and Exhibition in China. Society of Petroleum Engineers, Beijing, China.

Kumar, H., Elsworth, D., Liu, J., Pone, D., Mathews, J.P., 2015. Permeability evolution of propped artificial fractures in coal on injection of CO2. J. Petrol. Sci. Eng. 133, 695–704.

Lacy, L.L., Rickards, A.R., Ali, S.A., 1997. Embedment and fracture conductivity in soft formations associated with hec, borate and water-based fracture designs. In: SPE Annual Technical Conference and Exhibition. Society of Petroleum Engineers, San Antonio, Texas.
Li, S., Tang, D., Pan, Z., Xu, H., Huang, W., 2013. Characterization of the stress sensitivity of pores for different rank coals by nuclear magnetic resonance. Fuel 111, 746–754.
Li, X., Feng, Z., Han, G., Elsworth, D., Marone, C., Saffer, D., Cheon, D.-S., 2016. Permeability evolution and proppant compaction in artificial fractures on green river shale. In: 50th U.S. Rock Mechanics/Geomechanics Symposium. American Rock Mechanics Association, Houston, Texas.
Li, X., Feng, Z., Han, G., Elsworth, D., Marone, C., Saffer, D., Cheon, D.-S., 2017. Permeability evolution of propped artificial fractures in green river shale. Rock Mech. Rock Eng. 50 (6), 1473–1485.
Liu, H.-H., Rutqvist, J., 2009. A new coal-permeability model: internal swelling stress and fracture–matrix interaction. Transport Porous Media 82 (1), 157–171.
Ma, Y., Pan, Z., Zhong, N., Connell, L.D., Down, D.I., Lin, W., Zhang, Y., 2016. Experimental study of anisotropic gas permeability and its relationship with fracture structure of Longmaxi shales, Sichuan Basin, China. Fuel 180, 106–115.
Man, S., Wong, R. Chik-Kwong, 2017. Compression and crushing behavior of ceramic proppants and sand under high stresses. J. Petrol. Sci. Eng. 158, 268–283.
McKee, C.R., Bumb, A.C., Koenig, R.A., 1988. Stress-dependent permeability and porosity of coal and other geologic formations. SPE Form. Eval. 3 (1), 81–91.
Mitra, A., Harpalani, S., Liu, S., 2012. Laboratory measurement and modeling of coal permeability with continued methane production: Part 1–laboratory results. Fuel 94, 110–116.
Mittal, A., Rai, C.S., Sondergeld, C.H., 2017. Laboratory investigation of proppant-pack conductivity: eagle ford and vaca muerta shale. In: SPE/AAPG/SEG Unconventional Resources Technology Conference. Unconventional Resources Technology Conference, Austin, Texas, USA.
Palisch, T.T., Duenckel, R.J., Bazan, L.W., Heidt, J.H., Turk, G.A., 2007. Determining realistic fracture conductivity and understanding its impact on well performance - theory and field examples. In: SPE Hydraulic Fracturing Technology Conference. ., Society of Petroleum Engineers, College Station, Texas, U.S.A.
Pangilinan, K.D., de Leon, A.C.C., Advincula, R.C., 2016. Polymers for proppants used in hydraulic fracturing. J. Petrol. Sci. Eng. 145, 154–160.
Raimbay, A., Babadagli, T., Kuru, E., Develi, K., 2016. Quantitative and visual analysis of proppant transport in rough fractures. J. Nat. Gas Sci. Eng. 33, 1291–1307.
Shamsi, M.M.M., Nia, S.F., Jessen, K., 2017. Dynamic conductivity of proppant-filled fractures. J. Petrol. Sci. Eng. 151, 183-193.7.
Shi, J.-Q., Durucan, S., 2010. Exponential growth in san juan basin fruitland coalbed permeability with reservoir drawdown: model match and new insights. SPE Reservoir Eval. Eng. 13 (6), 914–925.
Tan, Y., Pan, Z., Feng, X.-T., Zhang, D., Connell, L.D., Li, S., 2019. Laboratory characterisation of fracture compressibility for coal and shale gas reservoir rocks: a review. Int. J. Coal Geol. 204, 1–17.
Tan, Y., Pan, Z., Liu, J., Feng, X.-T., Connell, L.D., 2018. Laboratory study of proppant on shale fracture permeability and compressibility. Fuel 222, 83–97.
Tan, Y., Pan, Z., Liu, J., Wu, Y., Haque, A., Connell, L.D., 2017. Experimental study of permeability and its anisotropy for shale fracture supported with proppant. J. Nat. Gas Sci. Eng. 44, 250–264.
Valdes, C., Heidari, Z., 2017. Application of nanoindentation for uncertainty assessment of elastic properties in mudrocks from micro- to well-log-scale. Geophysics 82, 1–58.
Volk, L.J., Raible, C.J., Carroll, H.B., Spears, J.S., 1981. Embedment of high strength proppant into low permeability reservoir rock. In: SPE/DOE Low Permeability Gas Reservoirs Symposium. U.S.A., Society of Petroleum Engineers, Denver, Colorado.
Wang, C., Zhang, J., Chen, J., Zhong, R., Cui, G., Jiang, Y., Liu, W., Chen, Z., 2021. Understanding competing effect between sorption swelling and mechanical compression on coal matrix deformation and its permeability. Int. J. Rock Mech. Min. Sci. 138, 104639.
Wang, C., Feng, J., Liu, J., Wei, M., Wang, C., Gong, B., 2014. Direct observation of coal–gas interactions under thermal and mechanical loadings. Int. J. Coal Geol. 131, 274–287.
Wang, C., Liu, J., Feng, J., Wei, M., Wang, C., Jiang, Y., 2016. Effects of gas diffusion from fractures to coal matrix on the evolution of coal strains: experimental observations. Int. J. Coal Geol. 162, 74–84.
Wang, J., Elsworth, D., 2018. Role of proppant distribution on the evolution of hydraulic fracture conductivity. J. Petrol. Sci. Eng. 166, 249–262.
Wen, Q., Zhang, S., Wang, L., Liu, Y., Li, X., 2007. The effect of proppant embedment upon the long-term conductivity of fractures. J. Petrol. Sci. Eng. 55 (3), 221–227.
Wu, Y., Pan, Z., Zhang, D., Down, D.I., Lu, Z., Connell, L.D., 2018. Experimental study of permeability behaviour for proppant supported coal fracture. J. Nat. Gas Sci. Eng. 51, 18–26.
Yang, M., Economides, M.J., 2012. Natural proppants for hydraulic fracture production optimization in barnett and eagle ford shales. In: SPE Western Regional Meeting. Society of Petroleum Engineers, Bakersfield, California, USA.
Zhang, F., Fang, Y., Elsworth, D., Wang, C., Yang, X., 2017. Evolution of friction and permeability in a propped fracture under shear. Geofluids 2017, 1–13.
Zheng, G., Pan, Z., Chen, Z., Tang, S., Connell, L.D., Zhang, S., Wang, B., 2012. Laboratory study of gas permeability and cleat compressibility for cbm/ecbm in Chinese coals. Energy Explor. Exploit. 30 (3), 451–476.
Zheng, W., Silva, S.C., Tannant, D.D., 2018. Crushing characteristics of four different proppants and implications for fracture conductivity. J. Nat. Gas Sci. Eng. 53, 125–138.
Zhi, S., Elsworth, D., 2020. Proppant embedment in coal and shale: impacts of stress hardening and sorption. Int. J. Coal Geol. 227, 103545.
Zuo, J., Lu, J., Ghandriz, R., Wang, J., Li, Y., Zhang, X., Li, J., Li, H., 2018. Mesoscale fracture behavior of Longmaxi outcrop shale with different bedding angles: experimental and numerical investigations. Int J Rock Mech Geotech 12, 297–309.